International Journal of Mechanical Sciences 316 (2026) 111470

Contents lists available at ScienceDirect

International Journal of Mechanical Sciences

journal homepage: www.elsevier.com/locate/ijmecsci

Soil surface erosion simulation using material point method

Hang Feng [a,b], Zhen-Yu Yin [a,b,*]

[a] Department of Civil and Environmental Engineering, The Hong Kong Polytechnic University, Hong Kong, China
[b] Research Institute for Land and Space, The Hong Kong Polytechnic University, Hong Kong, China

ARTICLE INFO

Keywords:
Material point method
Geomechanics
Constitutive model
Surface erosion
Bed-load
Suspended-load

ABSTRACT

Existing continuum-based soil surface erosion modeling has primarily focused on one-phase Eulerian methods, while the use of Lagrangian particle methods, particularly the Material Point Method (MPM), remains limited. Although two-phase MPM formulations for soil-water coupling have been developed, they typically employ conventional elastoplastic soil models that fail to capture the complex soil behavior involving transitions from a static bed to bed-load and suspended-load states. Furthermore, rigorous experimental validation and detailed comparative assessments of MPM for soil surface erosion remain scarce and underexplored. To address these gaps, this study applies the explicit two-phase two-point MPM algorithm to model the soil surface erosion. By employing dual sets of Lagrangian material points on a shared Eulerian grid, the approach effectively resolves soil-fluid interactions during erosion. An effective inflow/outflow boundary algorithm is proposed, enabling the addition and removal of water particles at the boundaries to achieve an efficient fluid boundary. Furthermore, a unified state-dependent constitutive framework for soil-solid is proposed, incorporating an elastoplasticity-$\mu(I)$ solid-to-fluid transition constitutive relation and an equation of state. The former captures the nonlinear solid-to-fluid transition behavior of bed-load particles, while the latter describes suspended-load particles. The proposed MPM model is validated against a series of benchmark problems, including dam break, water injection, wall-jet erosion, overtopping erosion, and tsunami overflow erosion scenarios. Comparative analysis demonstrates that the proposed MPM-based surface erosion model accurately captures the soil-fluid interface, bed-load, and suspended-load particle evolution in surface erosion without empirical erosion criteria.

1. Introduction

Soil surface erosion, a ubiquitous phenomenon across diverse natural and engineering systems, mainly refers to the process by which soil particles taken away by the flowing water [1–3]. This phenomenon is significant in many scenarios: (i) riverbed erosion, where sustained sediment transport reshapes fluvial landscapes [4–6]; (ii) overtopping erosion of earth dams and levees, has posed catastrophic threats to lives and infrastructures [7–9]; (iii) tsunami-induced erosion, where tsunami-induced overflow destabilizes breakwaters through rapid soil entrainment [10–12]. Given the significant influence of soil surface erosion on natural and engineering systems, it is essential to investigate soil surface erosion.

According to Liu et al. [13] and Feng et al. [14], the evolution of surface erosion can be classified into three distinct stages: (i) Initiation, where soil particles begin to detach from the soil bed as hydrodynamic forces exceed the resisting forces acting on individual grains [15–17]; (ii) Transport, during which mobilized particles transport either as bed load (i.e., moving by rolling, sliding, or saltation along the bed) or as suspended load (i.e., entrained within the fluid flow) [18–21]; and (iii) Sedimentation, where particles cease movement and settle onto the bed surface. During this multi-stage process, the complicated soil-fluid interactions and inter-soil-particle interactions basically govern the continuous morphological evolution of the soil surface.

To investigate the fundamental mechanisms of soil surface erosion, two primary experimental approaches are commonly employed: small-scale element tests and large-scale flume experiments. Small-scale element tests typically focus on the micro-mechanical responses of sediment beds under controlled loading conditions. In recent years, Cúñez et al. [16] examined the response of the granular bed to cyclic fluid-shear stresses of varying magnitudes and directions. Dasent et al. [22] used microtomography to characterize the internal structural evolution of granular media subjected to shear. Bodek et al. [23] conducted laboratory experiments demonstrating that stress history is stored anisotropically within sediment beds. Collectively, these studies emphasize that granular materials can exhibit distinct mechanical states

* Corresponding author.
E-mail addresses: fenghang.feng@connect.polyu.hk (H. Feng), zhenyu.yin@polyu.edu.hk (Z.-Y. Yin).

https://doi.org/10.1016/j.ijmecsci.2026.111470
Received 16 October 2025; Received in revised form 3 February 2026; Accepted 2 March 2026
Available online 5 March 2026

during soil surface erosion. In particular, bed-load transport may involve transitions between solid-like and fluid-like behavior, which can be interpreted by the framework of shear jamming [16,23]. However, despite their value for fundamental understanding, these small-scale tests are intrinsically limited in the spatial condition and cannot fully capture deformation and erosion processes at large, engineering-relevant scales.

Large-scale flume experiments (e.g., [24–27]) are conducted at or near engineering scale and are capable of reproducing the morphodynamical evolution of erosion surface under controlled hydraulic conditions. Although these experiments have provided important insights into the mechanics of soil surface erosion, they are constrained by issues of cost, reproducibility, and scalability to field conditions. Consequently, numerical methods that can represent the multi-state mechanical response of soil (e.g., solid-like and fluid-like behavior during bed-load transport) emerge as effective candidates for complementing and extending experimental investigations.

In recent years, a widely adopted approach is to directly model the microscopic behaviors of soil-water mixtures. This is typically achieved using the discrete element method (DEM), which explicitly represents particle-particle contact interactions. Building on this concept, several coupled numerical frameworks have been developed for surface erosion, such as LBM-DEM [28], CFD-DEM [29–31], and SPH-DEM [32–34]. These models excel at accurately representing the complex interactions between fluid and particles, as well as the inter-soil-particle dynamics. However, their application to large-scale and long-term engineering problems remains limited due to the substantial computational resources required to resolve the behavior of vast numbers of soil particles [35]. In contrast, continuum mechanics-based approaches offer a promising candidate for large-scale simulations, providing efficient and practical estimations for engineering applications. Motivated by these considerations, the continuum method is employed in this study.

To the authors' knowledge, a rational continuum method for modeling surface erosion should effectively capture the following four key mechanisms, as highlighted by our previous review (see [36]): **(i) The fluid domain**, requiring the numerical model to represent free surface and large deformation characteristics; **(ii) The soil domain**, which similarly demands accurate modeling of large deformations and free surfaces, but also necessitates a rational constitutive model to account for soil's multi-stage transitions (i.e., from static bed to bed-load and suspended-load); **(iii) Soil-fluid interaction terms**, which govern the momentum exchange between soil and fluid; and **(iv) The evolution of the soil-fluid interface**, representing erosion morphology, which is of primary engineering concern.

In developing reliable surface erosion models, existing continuum approaches primarily adopt either one-phase or two-phase formulations. Focusing on erosion morphology, one-phase models solve only the Navier-Stokes equations for fluid flow and approximate sediment transport using empirical formulae to update the bed surface [37–42]. While these models are computationally efficient and can capture the fluid domain and soil-fluid interface evolution (i.e., mechanisms (i) and (iv) discussed above), they inherently neglect solid-phase mechanics and soil-fluid interactions (mechanisms (ii) and (iii) discussed above). Moreover, their dependence on empirical relationships restricts their applicability to specific conditions [36].

In contrast, two-phase models treat the sand-water mixture as two interacting continua using volume-averaging techniques ([35,43]; see also Section 2). By solving two sets of mass and momentum equations for both soil and water, this framework offers a more comprehensive and physically consistent description, rigorously capturing all four critical mechanisms.

Within the two-phase modeling framework, each phase can be discretized using either Eulerian or Lagrangian numerical schemes. The Eulerian approach, such as the Finite Volume Method (FVM) and Finite Difference Method (FDM), is well established in Computational Fluid Dynamics (CFD) (see [44]). In contrast, Lagrangian particle methods, including Smoothed Particle Hydrodynamics (SPH) (e.g., [45]), Material Point Method (MPM) (e.g., [46]), Peridynamics (PD) (e.g., [47]), Moving Particle Semi-implicit (MPS) (e.g., [2,48]), Consistent Particle Method (CPM) (e.g., [49]), and Particle Finite Element Method (PFEM) (e.g., [50]), are particularly effective for problems involving large deformations and free surfaces. Among these methods, SPH, PD, MPS, and CPM are fully meshless, relying on various kernel or weight functions for field approximation. In contrast, PFEM and MPM are particle-mesh hybrid methods, utilizing both particles and a background grid to solve the momentum equation. Their primary distinction lies in mesh treatment: MPM employs a fixed computational grid, whereas PFEM uses a moving mesh that requires a remeshing technique to conform to material deformation.

Based on the numerical treatment of fluid and solid phases, two-phase surface erosion models can be categorized as: (i) Eulerian models, where both phases are solved using Eulerian methods (e.g., [51–53]); (ii) hybrid models, which combine an Eulerian approach for the fluid phase with a Lagrangian particle method for the soil-solid phase (e.g., FVM-MPM by [35]); and (iii) Lagrangian particle models, where both phases are treated with Lagrangian particle methods (e.g., [54–56,49,57–59]). Among these, fully Lagrangian particle formulations show significant potential to seamlessly capture all four critical mechanisms within a unified framework. However, their development remains ongoing in the current literature.

Recent advances in Lagrangian particle methods for surface erosion modeling have primarily adopted two approaches for representing the erosion surface: explicit and implicit procedures. Notably, this distinction pertains to the description of the erosion surface, rather than time integration schemes. Most Lagrangian particle methods employ the explicit approach (see Table 1), with notable examples including SPH [57] and PFEM [54,55]. In these methods, the governing equations do not follow the classical two-phase flow framework (see Section 2), and the solid and fluid phases are not fully coupled. Specifically, the solid phase is modeled as discrete particles, while the fluid phase is governed by the Navier-Stokes equations. The erosion surface is explicitly tracked by removing solid particles or elements at the interface based on empirical criteria, such as the Shields number [54,57] or critical frictional work [55]. While computationally efficient, this approach inherently neglects key aspects of solid-phase mechanics and soil-fluid interactions (mechanisms (ii) and (iii)).

The implicit representation of erosion morphology in Lagrangian particle methods is grounded in the volume-averaged two-phase flow framework (see Section 2), where the solid and fluid phases are fully coupled. In this approach, the erosion surface emerges implicitly by solving the coupled mass and momentum equations for both soil and water, rather than by explicitly removing solid particles. Currently, few

Table 1
Existing particle-based methods for surface erosion simulation.

Numerical method	Obtaining the erosion surface	Detailed description	Reference	Strict physical mechanism
PFEM	Explicit	The deletion of soil particle	[55]	×
PFEM	Explicit	The deletion of soil particle	[54]	×
SPH	Explicit	The deletion of soil particle	[57]	×
SPH	Implicit	The solution of the two-phase flow model	[58]	×
MPM	Implicit	The solution of the two-phase flow model	[60]	×
This study	Implicit	The solution of the two-phase flow model	-	√

methods employ this approach; notable examples include the MPM model by Yamaguchi et al. [61] and Liang et al. [60] and the SPH model by Zhou et al. [58].

Focusing on the Material Point Method (MPM), which combines an Eulerian grid with Lagrangian material points to solve the weak-form governing equations, this method has been widely adopted for simulating large deformations in soil mechanics. Recent studies have extended MPM to two-phase formulations for soil-water coupling problems [62–66], and these formulations have been employed for cases such as water-jet-soil interactions [67], debris flows [68], and submarine landslides [69]. However, the application of MPM to surface erosion modeling remains limited and underexplored. Although some studies have attempted to simulate overtopping using MPM [60,61,64,66], these works apply the two-phase MPM only to simple surface erosion cases such as overtopping, and employ a traditional elastoplastic model for soil. This approach reduces the accuracy of representing both bed-load and suspended-load particle behavior, and it fails to capture the complex response of granular soils in different states (e.g., transitions between solid-like and fluid-like behavior) that occur during soil surface erosion. In addition, these studies lack rigorous validation against experimental data and do not provide a comprehensive analysis of the two-phase MPM algorithm for soil surface erosion. The development of an accurate and efficient MPM model for surface erosion is still hindered by some key challenges, such as capturing complex particle-particle interactions and the multi-stage transitions of soil particles, and devising robust algorithms for fluid inflow and outflow boundary conditions.

To this end, this study puts forward an innovative surface erosion model based on the material point method. We extend the two-phase two-point MPM with the explicit time integration, which effectively resolves complex soil-water interactions during surface erosion. Unlike previous studies, we employ an inflow/outflow boundary algorithm for the fluid solver within the MPM framework, enabling accurate and efficient representation of fluid boundaries. Furthermore, to capture intricate particle-particle interactions and the multi-stage transitions of soil particles, we introduce a unified state-dependent constitutive framework that describes the multi-stage stress evolution of soils. Specifically, a critical-state-based elastoplastic-$\mu(I)$ solid-to-fluid constitutive relation [14] is employed to represent bed-load particles as granular flows, while suspended-load states are modeled using the water's equation of state for simplicity. The performance of the proposed MPM in capturing the evolution of the soil-fluid interface during surface erosion is validated through a series of experimental benchmarks. The advantages and limitations of the new MPM model are also discussed.

The structure of the following paper is organized as follows: Section 2 describes the governing equations in the two-phase saturated soil model, followed by a detailed description of the proposed constitutive model for water and soils in Section 3. Section 4 further presents the numerical implementation of explicit two-phase two-point MPM. Numerical examples validating the proposed MPM-based surface erosion model are provided in Section 5. Section 6 discusses the advantages and shortcomings of the developed MPM model. Finally, Section 7 summarizes the main conclusions of the study.

2. Conservation equations

Developing a realistic numerical solver for surface erosion fundamentally relies on the accuracy of its underlying mathematical model. In the current literature, mathematical models for surface erosion are broadly categorized into physics-based and empiricism-based approaches [36]. In this study, we concentrate on the physics-based models, with a particular emphasis on the two-phase saturated soil framework, which captures the macroscopic behavior of soil-water mixtures. This approach has gained prominence due to its ability to effectively represent the complex interactions between soil particles and fluids during the erosion process. For a comprehensive overview of the governing equations and recent advancements in this area, readers are referred to the detailed review by Feng et al. [36].

Accordingly, this section mainly discusses the two-phase governing equations, including the notation system, the volume-averaging technique, and the conservation equation.

2.1. Notation

A consistent notation system is adopted throughout this paper to represent various mathematical symbols. Specifically, scalar variables are denoted by non-bold symbols, vector variables by bold lowercase letters, and matrix variables by bold uppercase letters. $\square_{sp}$ and $\square_{wp}$ are the variables of the soil-solid and water particle, respectively. $\square_{sI}$ and $\square_{wI}$ are the variables of the soil-solid and water nodes, respectively. $\square^{k}$ and $\square^{k+1}$ are the variables at the k step and $k+1$ step, respectively. $\dot{\square}$ and $\ddot{\square}$ represent the first and second-order material time derivatives, respectively. $\square \cdot \square$ denotes the single dot product; $\square : \square$ denotes the double dot product.

2.2. Volume-averaging technique

As discussed in the introduction part, surface erosion can be conceptualized as the detachment and transport of discrete soil-solid particles within a fluid medium, forming a soil-water mixture. This mixture is described using the following assumptions in this study: (i) The system comprises only solid particles and fluid, and air is neglected; (ii) Solid particles exhibit uniform density ρ_s and diameter d, with the volume expressed as V_s=$n_s V$; (iii) The fluid exhibits uniform density ρ_w, with the volume expressed as V_w=$n_w V$. The basic volume equation is given as follows:

$$V = V_w + V_s = n_w V + n_s V \tag{1}$$

where V is the volume of the soil-water mixture; n_w is the fluid volume fraction; n_s is the solid volume fraction (n_w+n_s=1); V_w and V_s are the volumes of the water and solid particles, respectively.

Given the discrete nature of soil solid particles, the Discrete Element Method (DEM) provides a conceptually rigorous modeling framework. However, DEM becomes computationally prohibitive for large-scale engineering systems. We therefore employ the volume-averaging technique [70–74] to transition the non-continuum soil-water mixture to a continuum representation, enabling the application of continuum mechanics-based conservation equations to both phases.

As illustrated in Fig. 1, this approach considers properties homogeneous within a Representative Elementary Volume (REV), while capturing averaged quantities variations at the macroscopic scale. The discrete soil particles are homogenized into a continuum solid phase whose effective density (i.e., volume-averaged density) is defined as follows:

$$\overline{\rho}_s = n_s \rho_s \tag{2}$$

where $\overline{\rho}_s$ is the volume-averaged density of the continuum solid phase.

Similarly, the interstitial fluid occupying pore spaces is homogenized into a continuum fluid phase with effective density defined as follows:

$$\overline{\rho}_w = n_w \rho_w \tag{3}$$

where $\overline{\rho}_w$ is the volume-averaged density of the continuum water phase.

2.3. Conservation equations

By applying the volume-averaging technique described above, the soil-water mixture undergoing surface erosion can be represented by two coupled sets of conservation equations. These equations govern the mass and momentum conservation for both the soil-solid phase and the fluid phase.

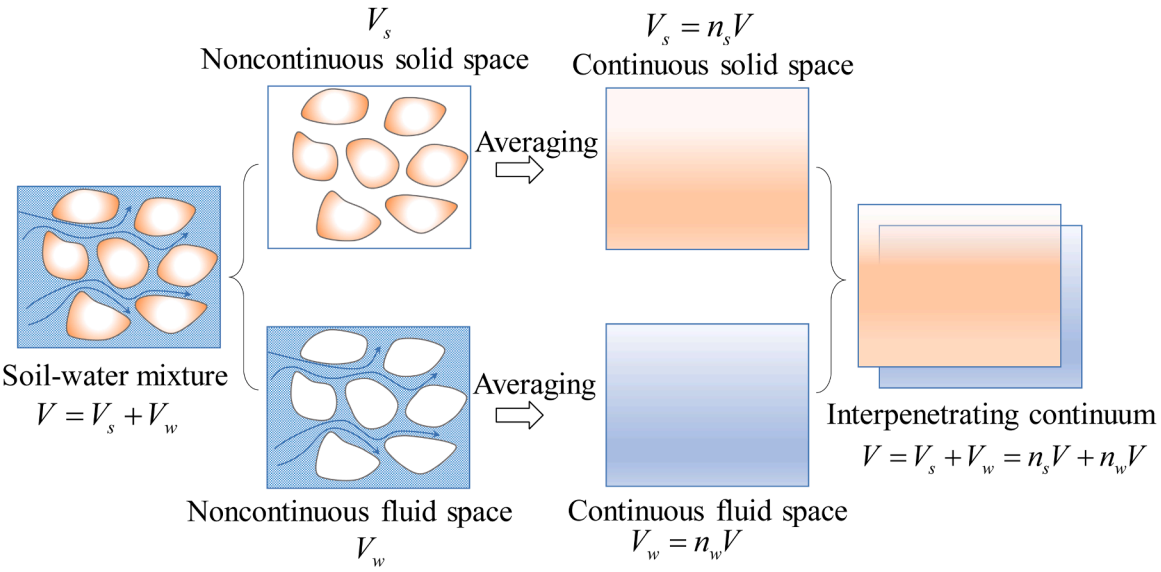

Fig. 1. The volume-averaging technique in the two-phase saturated soil model.

In the Lagrangian form, conservation equations of the fluid phase are described as follows:

$$\frac{d\overline{\rho}_w}{dt} = \frac{d(n_w\rho_w)}{dt} = -\nabla\cdot(n_w\rho_w\mathbf{v}_w) \tag{4}$$

$$n_w\rho_w\dot{\mathbf{v}}_w = \nabla\cdot\overline{\boldsymbol{\sigma}}_w + n_w\rho_w\mathbf{b} - \mathbf{f}^i \tag{5}$$

where $\mathbf{v}_w$ is the velocity of the fluid phase; $\mathbf{b}$ denotes the body force; $\overline{\boldsymbol{\sigma}}_w$ is the volume-averaging fluid stress; $\mathbf{f}^i$ represents the solid-fluid coupling term.

In the Lagrangian form, conservation equations of the soil-solid phase are described as follows:

$$\frac{d\overline{\rho}_s}{dt} = \frac{d(n_s\rho_s)}{dt} = -\nabla\cdot(n_s\rho_s\mathbf{v}_s) \tag{6}$$

$$n_s\rho_s\dot{\mathbf{v}}_s = \nabla\cdot\overline{\boldsymbol{\sigma}}_s + n_s\rho_s\mathbf{b} + \mathbf{f}^i \tag{7}$$

where $\mathbf{v}_s$ is the velocity of the solid phase; $\overline{\boldsymbol{\sigma}}_s$ is the volume-averaging soil-solid phase stress, which is discussed in the Section 3.

The above original conservation equations can be simplified using the following assumptions:

(i) The soil solid particle is incompressible, and the gradient of porosity is neglected. Under these conditions, the soil-solid mass conservation equation is restated as:

$$\frac{dn_s}{dt} = -n_s\nabla\cdot(\mathbf{v}_s) \tag{8}$$

(ii) We neglect the density gradient of water and treat water as weakly compressible. Accordingly, the fluid-phase mass conservation equation reduces to:

$$\frac{1}{\rho_w}\frac{d\rho_w}{dt} = -\frac{1}{n_w}[n_s\nabla\cdot(\mathbf{v}_s) + n_w\nabla\cdot(\mathbf{v}_w)] \tag{9}$$

(iii) The solid-fluid interaction force: The interaction force between solid and fluid phases in porous media is commonly described by two models: the linear Darcy's law and the nonlinear Darcy-Forchheimer law. While Darcy's law is widely applied for its simplicity, its validity is limited to low Reynolds number flows, where it accurately represents the proportional relationship between hydraulic gradient and flow velocity. At higher seepage velocities, inertial effects become significant, causing Darcy's model to deviate from experimental observations. The Darcy-Forchheimer law addresses this limitation by incorporating an additional quadratic velocity term, thereby capturing both the linear viscous drag and nonlinear inertial resistance. Consequently, it is the preferred formulation for modeling high-velocity flow regimes in porous media.

A detailed discussion of this term can be found in Zou et al. [75]. Following their formulation, a physically-consistent expression for the solid-fluid interaction force is provided by the Darcy-Forchheimer relation, which is given as follows:

$$\nabla p = \frac{\mu_w}{\kappa}q + \frac{\rho_w}{\kappa_1}q^2 \tag{10}$$

where μ_w is the dynamic viscosity (Pa•s); κ is the absolute permeability (m^2); κ_1 is the inertial permeability (m); q is the flux of fluid (m/s); κ, κ_1, and q are expressed as follows:

$$\kappa = \frac{d^2}{150}\frac{{n_w}^3}{(1-n_w)^2} \tag{11}$$

$$\kappa_1 = \frac{d}{1.75}\frac{{n_w}^3}{1-n_w} \tag{12}$$

$$q = n_w(\mathbf{v}_w - \mathbf{v}_s) \tag{13}$$

where d is the solid particle diameter.

Substituting Eqs. (11)-(13) into Eq. (10) and replacing the pressure drop using the solid-fluid interaction force $\mathbf{f}^i$, we obtain:

$$\mathbf{f}^i = \frac{\mu_w}{{n_w}^2}\frac{150}{d^2}(1-n_w)^2(\mathbf{v}_w - \mathbf{v}_s) + \frac{1.75}{d}\frac{\rho_w}{n_w}(1-n_w)|(\mathbf{v}_w - \mathbf{v}_s)|(\mathbf{v}_w - \mathbf{v}_s) \tag{14}$$

In addition, effective numerical simulation of surface erosion requires accurate solutions to the governing equations across both spatial and temporal domains (i.e., in space $\Omega_w, \Omega_s \subseteq \mathbb{R}^3$ and in time $t \in [0, T]$), complemented by the application of appropriate boundary conditions. In this study, we primarily employ Dirichlet and Neumann boundary conditions, which are defined as follows:

$$\begin{cases} \mathbf{x}_w = \bar{\mathbf{x}}_w on \Gamma_w^D \\ \boldsymbol{\sigma}_w \cdot \mathbf{n} = \bar{\mathbf{t}}_w on \Gamma_w^N \end{cases} \tag{15}$$

$$\begin{cases} \mathbf{x}_s = \bar{\mathbf{x}}_s on \Gamma_s^D \\ \boldsymbol{\sigma}_s \cdot \mathbf{n} = \bar{\mathbf{t}}_s on \Gamma_s^N \end{cases} \tag{16}$$

where Γ_w^D and Γ_w^N are the Dirichlet and Neumann boundaries of the water phase, respectively;Γ_s^D and Γ_s^N are the Dirichlet and Neumann boundaries of the solid phase, respectively. Both Dirichlet and Neumann boundaries are subsets of the domain boundary, defined as $\Gamma_w^D \cap \Gamma_w^N = \varnothing$ and $\Gamma_w^D \cup \Gamma_w^D = \partial\Omega_w$; $\Gamma_s^D \cap \Gamma_s^N = \varnothing$ and $\Gamma_s^D \cup \Gamma_s^D = \partial\Omega_s$. $\mathbf{n}$ is the outward unit normal vector; $\bar{\mathbf{x}}_w$ is the prescribed displacement on the water Dirichlet boundary; $\bar{\mathbf{t}}_w$ is the prescribed traction on the water Neumann boundary; $\bar{\mathbf{x}}_s$ is the prescribed displacement on the solid Dirichlet boundary; $\bar{\mathbf{t}}_s$ is the prescribed traction on the solid Neumann boundary.

Remark 1. The above volume-averaged two-phase saturated soil model may have some limitations: (i) interparticle interactions are indirectly expressed via an averaged soil constitutive model, while particle-fluid interactions rely on the empirical Darcy-Forchheimer relation, omitting particle-fluid forces such as virtual mass force, Basset force, Saffman force, and Magnus force (see [36]); (ii) the averaging volume magnitude often deviates significantly from point-scale volumes, inadequately resolving velocity fluctuations at a smaller scale. Consequently, this framework lacks generalizability across broad and dispersed solid concentrations [72]. Nevertheless, it remains effective and computationally efficient for characterizing the macroscopic behavior of soil-water mixtures in surface erosion. Hence, numerous studies adopt it for simulations.

3. Constitutive models

To close the above conservation equations, suitable constitutive models are required. The models for water and soils are discussed in detail in this section.

3.1. Equation of state for water

The fluid phase exhibits no history-dependent behavior and can therefore be described using a Newtonian rheology model. Accordingly, the volume-averaged fluid phase stress $\bar{\boldsymbol{\sigma}}_w$ is expressed as follows:

$$\bar{\boldsymbol{\sigma}}_w = -n_w p_w \mathbf{I} + \mathbf{s}_w \tag{17}$$

$$\mathbf{s}_w = \mu_w \left(\nabla \cdot \mathbf{v}_w + (\nabla \cdot \mathbf{v}_w)^T \right) \tag{18}$$

where $\mathbf{I}$ is the identity tensor; p_w represents the pore pressure, with compression considered as positive; $\mathbf{s}_w$ presents the fluid viscous stress.

The fluid phase is considered a weakly compressible fluid, its pressures is controlled by the equation of state, which is given as follows:

$$p_w = B\left(\left(\frac{\rho_w}{\rho_{w0}} \right)^{\gamma} - 1 \right) \tag{19}$$

where ρ_{w0} is the reference density of water; B is the parameter defined as $B = c_s^2 \rho_{w0} / \gamma$; c_s is the speed of sound related to the inflow water velocity, defined as $c_s = 10|\mathbf{v}_w|$ ($|\mathbf{v}_w|$ is the inflow water velocity magnitude); γ is taken as 7 in this study.

3.2. State-dependent constitutive framework for soils

The volume-averaged soil solid phase stress $\bar{\boldsymbol{\sigma}}_s$ is expressed as follows:

$$\bar{\boldsymbol{\sigma}}_s = \boldsymbol{\sigma}' - n_s p_w \mathbf{I} = \boldsymbol{\sigma}' - (1 - n_w) p_w \mathbf{I} \tag{20}$$

where $\boldsymbol{\sigma}'$ presents the effective stress, which can behave as solid-like or fluid-like states.

As discussed before, surface erosion is divided into three distinct regimes: initiation (i.e., onset of particle motion), transport (i.e., bed-load or suspended-load movement), and sedimentation. Accordingly, the granular particles can be simplified into three states (see Fig. 2): (i) non-eroded particles, representing a solid-like granular assembly; (ii) bed-load particles, corresponding to a fluid-like granular assembly; and (iii) suspended-load particles, which are granular particles fully surrounded by water. Based on this simplification, surface erosion can be viewed as a complex phase transition from the non-eroded state to the eroded state (i.e., bed-load or suspended-load). Consequently, describing the effective stress of soils requires a state-dependent constitutive model that can uniquely capture the mechanical behavior of three particle states.

To describe the stress in the different types of soil particles described above, we develop a state-dependent constitutive framework for soils undergoing surface erosion (see Fig. 3), in which the constitutive relationship is governed by particle concentration. As concentration decreases during erosion, the soil transitions through three distinct phases (Fig. 3c):

(i) High concentration (non-eroded regime): Soil particles form a percolating solid skeleton. The mechanical behavior can be effectively described using models from geotechnical engineering, such as elastoplastic frameworks (e.g., [76–78]) and hypoplastic models (e.g., [79,80]).
(ii) Intermediate concentration (bed-load regime): In this regime, soil particles move collectively in granular assemblies along the erosion surface. To capture the shear-dependent frictional characteristics of granular flows, non-Newtonian rheology models are required. Several phenomenological rheology models have been developed for this purpose (e.g., [81–83]).
(iii) Low concentration (suspended-load regime): Soil particles are nearly fully surrounded by water, which can be assumed as a Newtonian fluid. The constitutive relationship for suspended-load particles thus differs from those in the previous two states and is assumed to be governed by the water's stress model described in Section 3.1.

Additionally, the above stages (i) and (ii) can be unified through a phase transition framework for granular flows. The transition from non-eroded particles (high solid concentration) to bed-loaded particles (intermediate concentration) can be regarded as a granular flow process [84,85]. To capture the complex evolution of effective stress during this transition (Fig. 3a), we employ a well-established critical-state-based elastoplastic-$\mu(I)$ solid-to-fluid transition constitutive relation [14]. This solid-fluid phase transition model, which has been rigorously validated via element tests and granular flow experiments, can explicitly describes the non-eroded to bed-loaded particle transition. A brief overview follows:

Fig. 3(a) illustrates the critical-state-based elastoplastic-$\mu(I)$ constitutive relation [14], which uses the critical state concept [86] as an initiation criterion to distinguish solid-like and fluid-like granular states. At the critical state, materials undergo continuous deformation without stress or volume changes. The model decomposes granular stress into: (i) a rate-dependent viscous stress (fluid-like state); (ii) a rate-independent elastoplastic component (solid-like state). The effective stress is expressed as follows:

$$\boldsymbol{\sigma}' = \boldsymbol{\sigma}_{ep} + \boldsymbol{\sigma}_v \tag{21}$$

where $\boldsymbol{\sigma}_{ep}$ represents the elastoplastic stress component; $\boldsymbol{\sigma}_v$ defines the viscous stress component. This constitutive relation is detailed in Appendix A for completeness. The key input parameters are summarized in

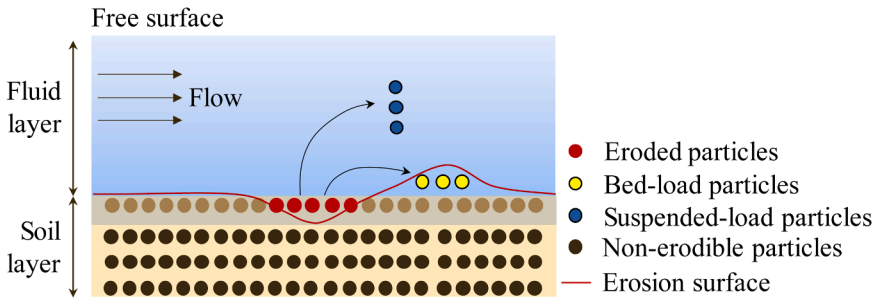

Fig. 2. Description of different types of soil particles during surface erosion.

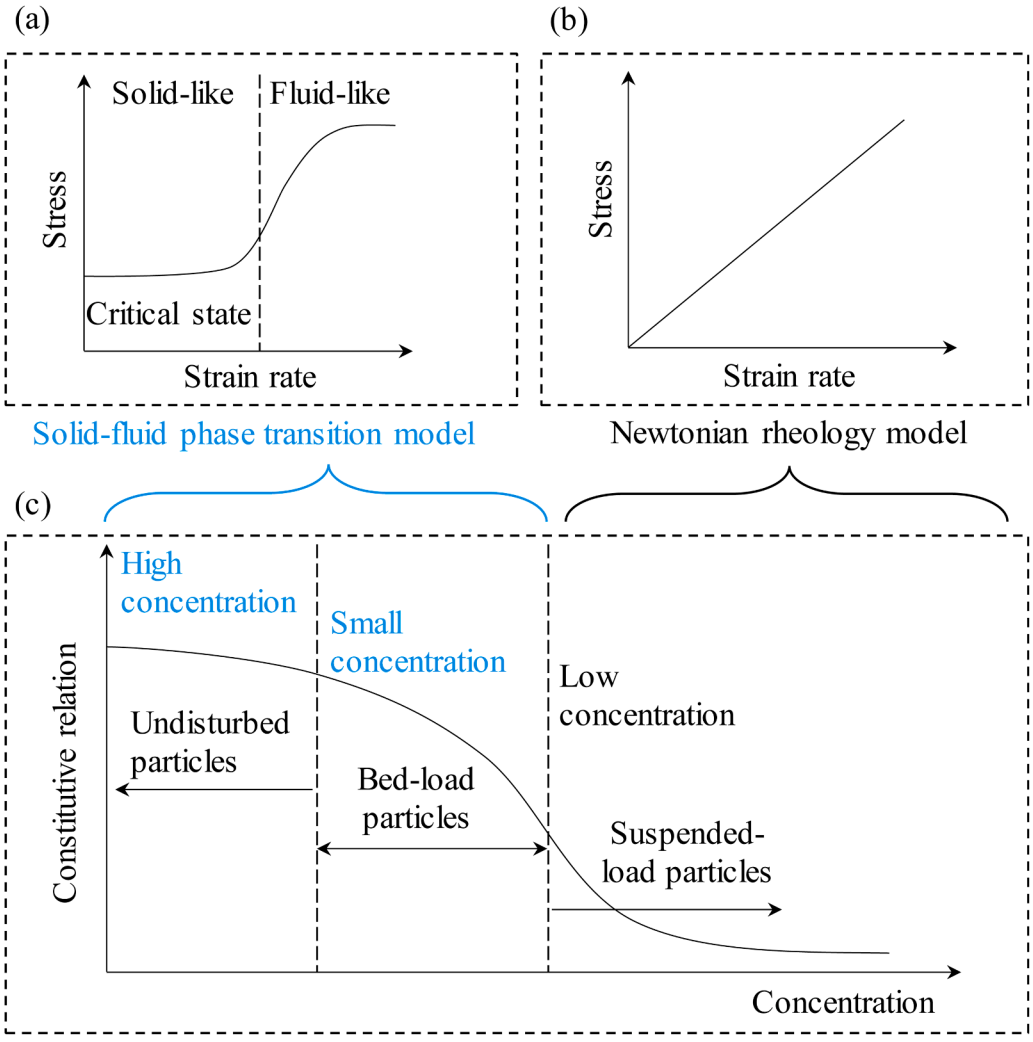

Fig. 3. The illustration of the soil's stress model during surface erosion. (a) The solid-fluid phase transition model; (b) Newtonian rheology model; (c) The non-linear constitutive relation during soil surface erosion.

Table 2.

In summary, we propose a state-dependent constitutive framework for soils in surface erosion (Fig. 3), which can be represented as a piecewise constitutive relation:

(i) For $n_s \leq n_{s,c}$ (i.e., solid concentrations below a critical value): the elastoplastic-$\mu(I)$ phase transition model describes both non-eroded particles (high concentration) and bed-load particles (intermediate concentration), unifying granular flow behavior.

(ii) For $n_s > n_{s,c}$ (i.e., solid concentrations exceeding a critical value): the water stress model in Section 3.1 governs suspended-load solid particles (high concentration).

In this study, the critical solid concentration $n_{s,c} = 0.4$ (void ratio $e = 1.5$) is adopted for all simulations. This value notably exceeds typical Random Loose Packing (RLP) void ratios ($e \approx 0.8 - 1.0$), intentionally allowing granular flows to persist beyond the RLP state. While this setting enables continuous modeling of the transition from the bed-load to suspended-load state, we acknowledge that precise determination of

Table 2
Basic input parameters in the proposed unified elastoplasticity-μ(I) model.

Stress type	Parameter	Definition	Example 3	Example 4	Example 5
Elastoplastic stress	E_0	Dimensionless referential elastic modulus	216	216	216
	ν	Poisson's ratio	0.2	0.2	0.2
	n	Constant controlling nonlinear elastic stiffness	0.50	0.5	0.5
	φ_c	Critical-state friction angle	35.00	30.00	30.00
	e_0	Initial void ratio	0.695	0.695	0.818
	e_{ref}	Initial critical-state void ratio	0.807	0.977	0.827
	λ	Constant controlling CSL nonlinearity	0.0596	0.0596	0.0596
	ξ	Constant controlling CSL nonlinearity	0.365	0.365	0.365
	A_d	Constant controlling stress dilatancy magnitude	0.7	0.7	0.7
	k_p	Plastic modulus–related constant	0.0044	0.044	0.0044
	n_p	Peak strength parameter	2.4	2.4	2.4
	n_d	Phase transformation parameter	2.9	2.9	2.9
Viscous stress	I_0	Referential inertial ratio	0.28	0.28	0.28
	ρ_s	Particle density (kg/m^3)	2650	2650	2650
	d	Particle diameter (m)	$0.85\bullet10^{-3}$	$1\bullet10^{-3}$	$2\bullet10^{-3}$
	μ_s	Static friction coefficient (tanφ)	0.700	0.577	0.577
	μ_d	Dynamic friction coefficient	0.770	0.660	0.660
	Φ_c	Random close volume fraction	0.70	0.70	0.70
	$\Delta\Phi$	Dynamic loosening factor	0.29	0.29	0.29

$n_{s,c}$ remains challenging, an inherent limitation of the current framework. Note that the calibration process of the constitutive parameters in the elastoplasticity-$\mu(I)$ model is discussed in this Appendix B.

4. Two-phase two-point material point method

In this section, the governing equations with effective boundary conditions are solved using the fully explicit two-phase two-point material point method.

4.1. Weak form and spatial discretization

To solve the momentum equations, the strong form is transferred into the weak form using the standard Galerkin method. This process mainly includes multiplying arbitrary test functions, applying Gauss's flux theorem, and conducting requisite mathematical operations. The final weak form for the water and solid phases is given as follows:

$$\int_{\Omega_w} \overline{\rho}_w \mathbf{a}_w \cdot \delta\mathbf{u}_w \, d\Omega = -\int_{\Omega_w} \overline{\boldsymbol{\sigma}}_w : \nabla\delta\mathbf{u}_w d\Omega + \int_{\Omega_w} \overline{\rho}_w \mathbf{b} \cdot \delta\mathbf{u}_w \, d\Omega - \int_{\Omega_w} \mathbf{f}^i \cdot \delta\mathbf{u}_w \, d\Omega + \int_{\Gamma_w^N} \mathbf{t}_w^n \cdot \delta\mathbf{u}_w d\Gamma \tag{22}$$

$$\int_{\Omega_s} \overline{\rho}_s \mathbf{a}_s \cdot \delta\mathbf{u}_s \, d\Omega = -\int_{\Omega_s} \overline{\boldsymbol{\sigma}}_s : \nabla\delta\mathbf{u}_s d\Omega + \int_{\Omega_s} \overline{\rho}_s \mathbf{b} \cdot \delta\mathbf{u}_s \, d\Omega + \int_{\Omega_s} \mathbf{f}^i \cdot \delta\mathbf{u}_s \, d\Omega + \int_{\Gamma_s^N} \mathbf{t}_s^n \cdot \delta\mathbf{u}_s d\Gamma \tag{23}$$

where Ω_w and Ω_s are the volume of the water phase and solid phase, respectively; $\delta\mathbf{u}_w$ and $\delta\mathbf{u}_s$ are the virtual test functions for the water phase and solid phase, respectively, depending on the unknown water and solid velocity field $\mathbf{u}_w$ and $\mathbf{u}_s$. These virtual test functions are treated as zero at the Dirichlet boundaries, i.e., $\delta\mathbf{u}_w = \mathbf{0}, on\Gamma_w^D; \delta\mathbf{u}_s = \mathbf{0}, on\Gamma_s^D$.

The above weak-form equations are discretized using the Material Point Method (MPM), which employs two complementary descriptions: moving Lagrangian material points and a fixed Eulerian grid. Material points carry all state variables (e.g., velocity, stress, and strain), while the grid is employed for solving the conservation equations. A dynamic mapping of information between Lagrangian material points and the Eulerian grid is performed through shape functions. Compared to conventional finite element methods (FEM), MPM can be regarded as a specialized Lagrangian FEM variant that replaces Gaussian quadrature with particle-based integration and incorporates remeshing at each computational step.

Following the MPM discretization, the water and solid continuum bodies can be defined as follows:

$$\Omega_w = \sum_{wp=1}^{N_{wp}} V_{wp} \tag{24}$$

$$\Omega_s = \sum_{sp=1}^{N_{sp}} V_{sp} \tag{25}$$

where V_{wp} and V_{sp} are volumes of the water and solid particle, respectively; N_{wp} and N_{sp} are the total water and solid particle numbers, respectively.

The transfer of physical properties between Lagrangian particles and Eulerian grid is conducted via shape functions, given as follows:

$$\mathbf{v}_{wp}^k = \sum_{I=1}^{n} N_{I,wp}^k \mathbf{v}_{wI}^k \tag{26}$$

$$\mathbf{v}_{sp}^k = \sum_{I=1}^{n} N_{I,sp}^k \mathbf{v}_{sI}^k \tag{27}$$

where $\mathbf{v}_{wp}^k$ and $\mathbf{v}_{sp}^k$ represent the velocities of the water and solid particles

at the step k, respectively; $\mathbf{v}_{wI}^k$ and $\mathbf{v}_{sI}^k$ denote the velocities of the water and solid nodes at the step k, respectively. $N_{I,wp}^k$ and $N_{I,sp}^k$ are the shape function between grid and water particle, solid particle, respectively. In this study, we employ the quadratic B-spline shape function, which is given as follows:

$$N(x) = \begin{cases} \frac{3}{4} - x^2, 0 \le |x| < \frac{1}{2} \\ \frac{1}{2}\left(\frac{3}{2} - |x|\right)^2, \frac{1}{2} \le |x| < \frac{3}{2} \\ 0, \frac{3}{2} \le |x| \end{cases} \tag{28}$$

where x is the distance between the particle and the grid node.

4.2. Two-point two-phase MPM scheme

Following the spatial discretization process described above, the momentum conservation equations for water and solid phases can be solved sequentially. Each phase is represented by its own set of individual particles, with the governing equations for each phase solved explicitly. The interaction between the water and solid phases is captured through a solid-fluid coupling term. This approach is commonly referred to as the two-point two-phase MPM scheme (see [63]). As illustrated in Fig. 4, the proposed two-phase two-point MPM provides a systematic framework for simulating surface erosion problems. Notably, this solver can be regarded as an enhanced version of the traditional one-phase one-point MPM, in which each computational step is extended from the single-phase to the two-phase context. This extension preserves algorithmic simplicity, facilitating straightforward implementation and coding.

As is seen in Fig. 4, the main steps in the two-phase two-point MPM include:

(a) Particle to Grid (i.e., P2G)

We first begin with transferring the particle information to grid nodes via the shape function; the main transferred information includes mass and momentum of solid and fluid Lagrangian particles. In this step, we first obtain the mass and velocity of water nodes (i.e., step (a1) in Fig. 4) via the following equations:

$$m_{wI}^k = \sum_{wp} N_{I,wp}^k \, m_{wp}^k \tag{29}$$

$$\mathbf{v}_{wI}^k = \left(\sum_{wp} N_{I,wp}^k m_{wp}^k \mathbf{v}_{wp}^k\right) \Big/ m_{wI}^k \tag{30}$$

The mass and velocity of the solid nodes are then expressed as follows (i.e., step (a2) in Fig. 4):

$$m_{sI}^k = \sum_{sp} N_{I,sp}^k \, m_{sp}^k \tag{31}$$

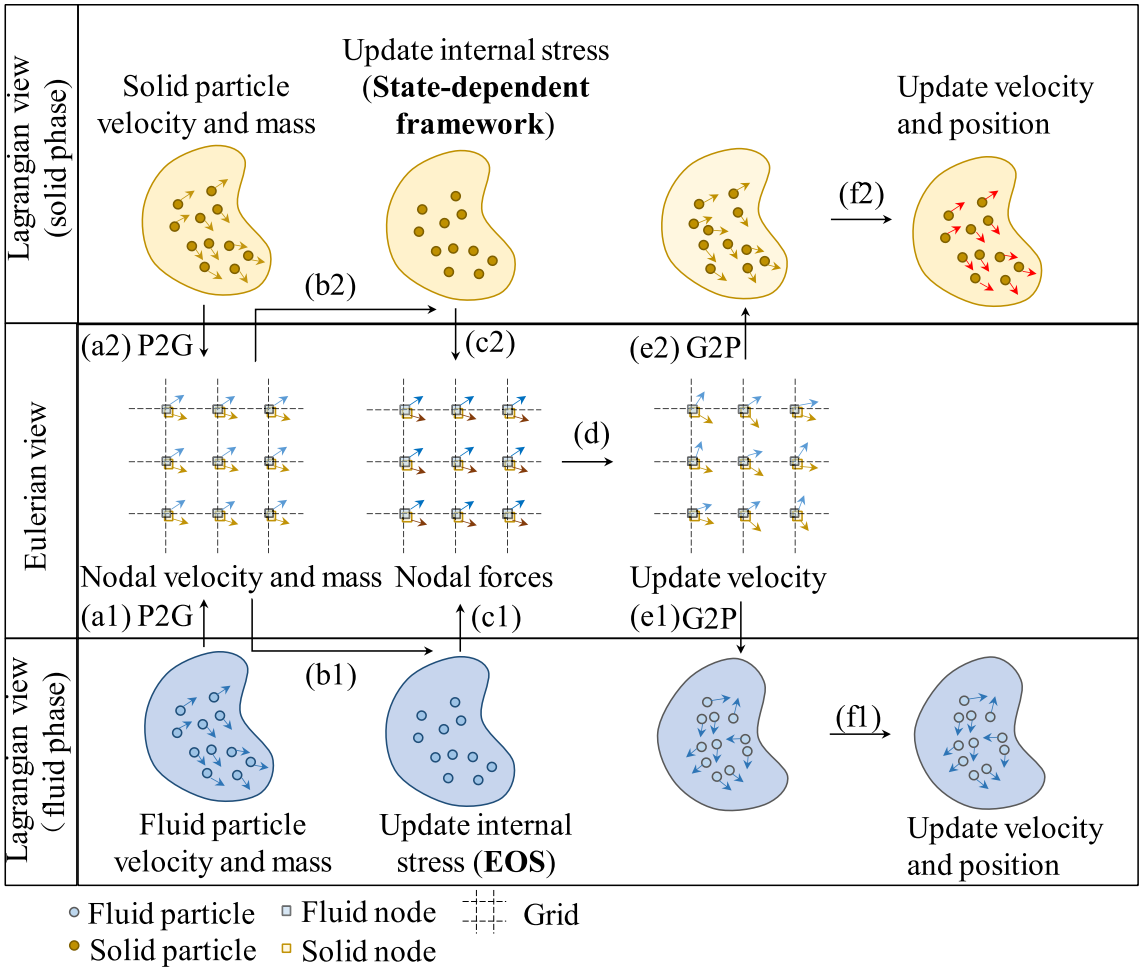

Fig. 4. The basic process of modeling soil surface erosion in the MPM.

$$\mathbf{v}_{sI}^{k}=\left(\sum_{sp}N_{I,sp}^{k}m_{sp}^{k}\mathbf{v}_{sp}^{k}\right)\Big/ m_{sI}^{k} \tag{32}$$

(b) Updating particle internal stress

In this step, the internal stress of the water particle is updated first (i.e., step (b1) in Fig. 4). This is achieved via updating the water particle's velocity gradient $\nabla\mathbf{v}_{wp}^{k}$, deformation gradient $\mathbf{F}_{wp}^{k}$, and strain tensor $\boldsymbol{\varepsilon}_{wp}^{k}$ using velocity information from the grid. Finally, the stress of the water particles is updated via the constitutive relation in Section 3.1. These equations are expressed as follows:

$$\nabla\mathbf{v}_{wp}^{k}=\sum_{I}\nabla N_{I,wp}^{k}\,\mathbf{v}_{wI}^{k} \tag{33}$$

$$\mathbf{F}_{wp}^{k}=\left(1+\nabla\mathbf{v}_{wp}^{k}\Delta t\right)\mathbf{F}_{wp}^{k-1} \tag{34}$$

$$\boldsymbol{\varepsilon}_{wp}^{k}=\frac{1}{2}\left(\mathbf{F}_{wp}^{k}+\left(\mathbf{F}_{wp}^{k}\right)^{T}\right)-\mathbf{I} \tag{35}$$

$$\boldsymbol{\sigma}_{wp}^{k}=f_{w}\left(\boldsymbol{\varepsilon}_{wp}^{k}\right) \tag{36}$$

where $\nabla\mathbf{v}_{wp}^{k}$ is the velocity gradient of the water particle at step k; $\mathbf{F}_{wp}^{k}$ and $\mathbf{F}_{wp}^{k-1}$ are the deformation gradient of the water particle at step k and k-1, respectively; $\boldsymbol{\varepsilon}_{wp}^{k}$ and $\boldsymbol{\sigma}_{wp}^{k}$ are the strain tensor and stress tensor of water particle, respectively; $f_{w}\left(\boldsymbol{\varepsilon}_{wp}^{k}\right)$ denotes the constitutive relation in Section 3.1.

Similar to the procedure used to update the internal stress of water particles, the internal stress of the solid particles is computed (i.e., step (a2) in Fig. 4) using the following equations:

$$\nabla\mathbf{v}_{sp}^{k}=\sum_{I}\nabla N_{I,sp}^{k}\,\mathbf{v}_{sI}^{k} \tag{37}$$

$$\mathbf{F}_{sp}^{k}=\left(1+\nabla\mathbf{v}_{sp}^{k}\Delta t\right)\mathbf{F}_{sp}^{k-1} \tag{38}$$

$$\boldsymbol{\varepsilon}_{sp}^{k}=\frac{1}{2}\left(\mathbf{F}_{sp}^{k}+\left(\mathbf{F}_{sp}^{k}\right)^{T}\right)-\mathrm{I} \tag{39}$$

$$\boldsymbol{\sigma}_{sp}^{k}=f_{s}\left(\boldsymbol{\varepsilon}_{sp}^{k}\right) \tag{40}$$

where $\nabla\mathbf{v}_{sp}^{t}$ is the velocity gradient of the solid particle at step k; $\mathbf{F}_{sp}^{k}$ and $\mathbf{F}_{sp}^{k-1}$ are the deformation gradient of the solid particle at step k and k-1, respectively; $\boldsymbol{\varepsilon}_{sp}^{k}$ and $\boldsymbol{\sigma}_{sp}^{k}$ are the strain tensor and stress tensor of the solid particle, respectively; $f_{s}\left(\boldsymbol{\varepsilon}_{sp}^{k}\right)$ denotes the state-dependent constitutive framework in Section 3.2. It should be noted that updating the internal stress using the solid-to-fluid transition constitutive relation involves a complex constitutive stress updating algorithm. In this study, an explicit stress updating algorithm is employed for this purpose (for details, see [14]).

(c) Updating grid forces

To solve the momentum equations for both the water and solid phases and obtain their respective velocity fields, it is necessary to calculate both the internal and external forces acting on each phase. The internal forces for the water and solid grids are updated using the following equations:

$$\mathbf{f}_{wI}^{int,\,k}=-\sum_{wp}\boldsymbol{\sigma}_{wp}^{k}\cdot\nabla N_{I,wp}^{k}\,V_{wp}^{k} \tag{41}$$

$$\mathbf{f}_{sI}^{int,\,k}=-\sum_{sp}\boldsymbol{\sigma}_{sp}^{k}\cdot\nabla N_{I,sp}^{k}\,V_{sp}^{k} \tag{42}$$

where $\mathbf{f}_{wI}^{int,\,k}$ and $\mathbf{f}_{sI}^{int,\,k}$ are the internal forces of the water and solid grids, respectively.

The external forces of water and solid grids are updated via the following equations:

$$\mathbf{f}_{wI}^{ext,\,k}=\sum_{wp}N_{I,wp}^{k}\,m_{wp}^{k}\,\mathbf{b}-\int_{\partial\Omega_{w}}\bar{\mathbf{p}}_{w}N_{I,wp}^{k}d\Gamma \tag{43}$$

$$\mathbf{f}_{sI}^{ext,\,k}=\sum_{sp}N_{I,sp}^{k}\,m_{sp}^{k}\,\mathbf{b}+\int_{\partial\Omega_{s}}\bar{\mathbf{t}}_{s}N_{I,sp}^{k}d\Gamma \tag{44}$$

where $\mathbf{f}_{wI}^{ext,\,k}$ and $\mathbf{f}_{sI}^{ext,\,k}$ are the external forces of the water and solid grids, respectively; $\bar{\mathbf{t}}_{s}$ denotes the surface force on the soil-solid phase; $\bar{\mathbf{p}}_{w}$ is the pressure vector on the boundary.

The solid-fluid coupling force is updated using equations below:

$$\mathbf{f}_{sI}^{d,k}=\mathbf{f}_{wI}^{d,k}=\frac{\mu_{w}}{\left(n_{wI}^{k}\right)^{2}}\frac{150}{d^{2}}\left(1-n_{wI}^{k}\right)^{2}\left(\mathbf{v}_{wI}^{k}-\mathbf{v}_{sI}^{k}\right)+\frac{1.75}{d}\frac{\rho_{w}}{n_{wI}^{k}}\left(1-n_{wI}^{k}\right)\left(\mathbf{v}_{wI}^{k}-\mathbf{v}_{sI}^{k}\right)\left|\mathbf{v}_{wI}^{k}-\mathbf{v}_{sI}^{k}\right| \tag{45}$$

where n_{wI}^{k} is the fluid volume fraction at the grid node.

The criterion determining whether the solid-fluid interaction force should be computed at the grid node is employed, which is expressed as follows:

$$\begin{cases} m_{sI}^{k}>0 \\ m_{wI}^{k}>0 \end{cases} \tag{46}$$

(d) Updating grid velocities

Since both the water and solid phases share the same grid, the velocities of the water and solid grids are updated using the following equations:

$$\mathbf{a}_{wI}^{k}=\frac{\mathbf{f}_{wI}^{int,\,k}+\mathbf{f}_{wI}^{ext,\,k}-\mathbf{f}_{wI}^{d,k}}{m_{sI}^{k}} \tag{47}$$

$$\mathbf{a}_{sI}^{k}=\frac{\mathbf{f}_{sI}^{int,\,k}+\mathbf{f}_{sI}^{ext,\,k}+\mathbf{f}_{sI}^{d,k}}{m_{sI}^{k}} \tag{48}$$

$$\mathbf{v}_{sI}^{k+1}=\mathbf{v}_{sI}^{k}+\mathbf{a}_{sI}^{k}\,\Delta t \tag{49}$$

$$\mathbf{v}_{wI}^{k+1}=\mathbf{v}_{wI}^{k}+\mathbf{a}_{wI}^{k}\,\Delta t \tag{50}$$

where $\mathbf{a}_{wI}^{k}$ and $\mathbf{a}_{sI}^{k}$ are the accelerations of water and solid grids, respectively; $\mathbf{v}_{sI}^{k}$ and $\mathbf{v}_{wI}^{k}$ are the velocities grids, respectively.

(e1, e2, f1, and f2) Grid to Particle (G2P) and updating positions

We obtain the updated particle velocity and position via interpola-

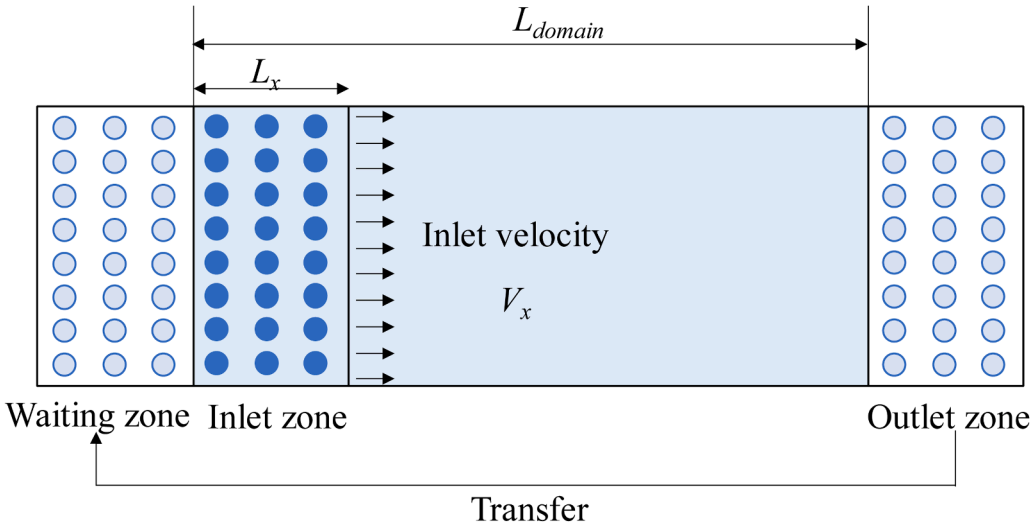

Fig. 5. The basic description of the boundary algorithm for inlet and outlet boundaries.

tion from the grid nodes, as follows:

$$\mathbf{v}_{sp}^{k+1} = \mathbf{v}_{sp}^{k} + \sum_I \mathbf{a}_{sI}^{k} N_{I,sp}^{k} \Delta t \tag{51}$$

$$\mathbf{v}_{wp}^{k+1} = \mathbf{v}_{wp}^{k} + \sum_I \mathbf{a}_{wI}^{k} N_{I,wp}^{k} \Delta t \tag{52}$$

$$\mathbf{x}_{sp}^{k+1} = \mathbf{x}_{sp}^{k} + \sum_I \mathbf{v}_{sI}^{k+1} N_{I,sp}^{k} \Delta t \tag{53}$$

$$\mathbf{x}_{wp}^{k+1} = \mathbf{x}_{wp}^{k} + \sum_I \mathbf{v}_{wI}^{k+1} N_{I,wp}^{k} \Delta t \tag{54}$$

Due to the fully explicit algorithm employed in this study, the critical time step is restricted by the stability condition. The method for calculating the critical time step is provided in Appendix C for completeness. Notably, the above two-phase two-point MPM algorithm is implemented using the in-house code developed by our group, rather than relying on commercial or open-source software. Specifically, this code is developed in Python to perform all simulations.

4.3. Inflow and outflow boundary algorithm

Unlike the algorithm proposed by Zhao et al. [87], the novel approach presented in this study enables the simulation of continuous flow with improved computational efficiency. It should be noted that inflow/outflow boundaries differ fundamentally from periodic boundaries. In a periodic system, the inflow and outflow of fluid are equal, forming a closed, mass-conserving cycle. In contrast, the inflow and outflow fluxes in the present model are prescribed independently and need not be equal. For this study, we employ inflow and outflow boundaries rather than periodic boundaries.

Fig. 5 illustrates the basic model setup with the inflow/outflow boundaries. The length of the computational domain is L_{domain}, while an inlet zone governing the inflow boundary is set within the computational domain with a length of L_x. The inlet zone employs the particle adding technique analogous to Zhao et al. [87], where new particles are introduced when the inlet zone is empty. Adding particles occurs at intervals determined:

$$dt = \frac{L_x}{V_x} \tag{55}$$

where L_x is the length of the inlet zone; V_x is the prescribed particle velocity during surface erosion; dt is the time interval for all the particle in the inlet zone run out.

Key innovation resides in the outflow treatment. Whereas Zhao et al. [87] permanently delete particles exiting the domain (see Eq. (56)), we implement a particle-recycling protocol. Outflow particles are redirected to a non-computational waiting zone instead of deletion. These particles are reintroduced at the inlet zone when the injection criterion (Eq. (55)) is satisfied, forming a closed-loop particle management system. This strategy eliminates repeated particle generation/deletion cycles, substantially reducing computational overhead while maintaining

Table 3
Summary of numerical examples with specific purposes in our previous studies or this study.

Aspects	Specific validation purpose	Reference
Solid	Performance of the solid-to-fluid transition constitutive relation	[14]
	Performance of the solid numerical solver	[14]
Fluid	Performance of the fluid numerical solver	Section 5.1
	Performance of the inflow/outflow boundary algorithm	Section 5.2
Surface erosion	Performance of the surface erosion solver (Small-scale short-term)	Section 5.3
	Performance of the surface erosion solver (Small-scale long-term)	Section 5.4
	Performance of the surface erosion solver (Large-scale long-term)	Section 5.5

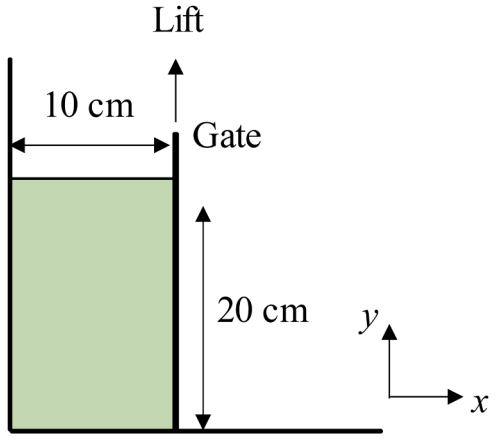

Fig. 6. The configuration of the dam break test.

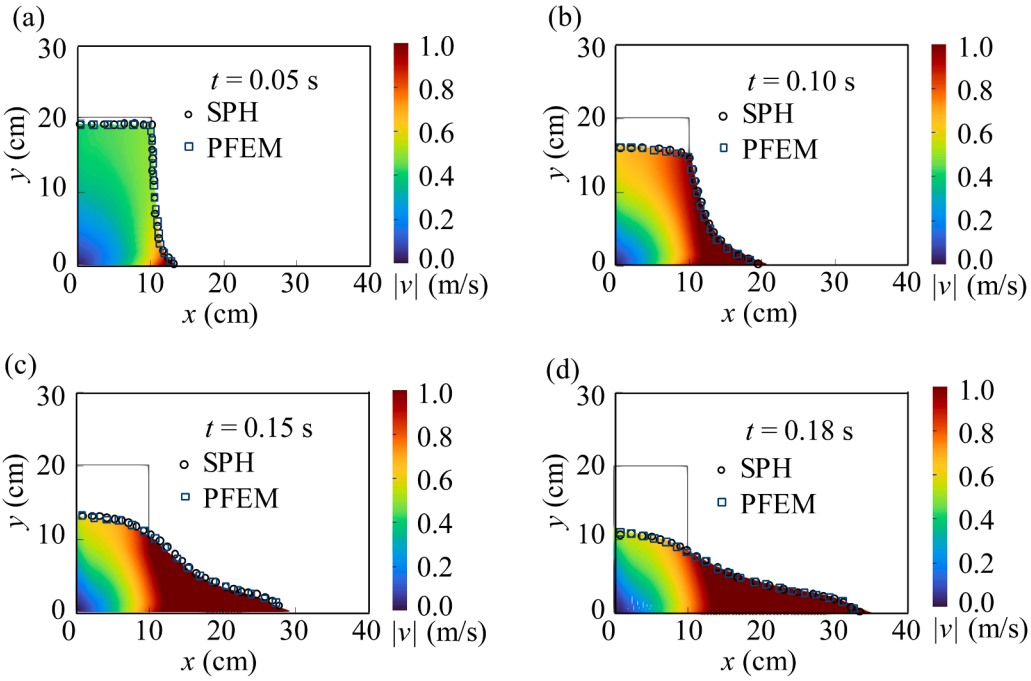

Fig. 7. Comparison between SPH results, PFEM results, and MPM results. (a) $t = 0.05$ s; (b) $t = 0.10$ s; (c) $t = 0.15$ s; (d) $t = 0.18$ s.

mass conservation.

$$x_{wp} > L_{domain} \tag{56}$$

where x_{wp} is x position of the water particle; L_{domain} is the length of the inlet zone.

5. Numerical examples

A series of numerical examples is employed to evaluate the performance of the proposed MPM-based surface erosion model across three aspects: pure soil domain, pure fluid domain, and solid-fluid coupling erosion (see Table 3). As the soil domain implementation, including the elastoplastic-$\mu(I)$ constitutive relation and soil-solid numerical solver, was validated previously [14], this study focuses on the fluid domain and solid-fluid coupling erosion mechanisms. Table 3 summarizes all test cases and their specific validation objectives. In all these examples, the Eulerian grid is discretized using a uniform structured rectangular element.

5.1. Example 1: water dam break

5.1.1. Model description

We first validate the fluid solver performance using a water dam break benchmark. As shown in Fig. 6, the initial configuration is characterized by a 10 cm × 20 cm (length × depth) water column restrained by a removable gate, consistent with the setup in Daly et al. [88]. Once the gate is rapidly lifted, the water dam collapses, generating the free-surface flows. During the simulation, the time step is set to 1×10^{-5} s to ensure computational convergence. The grid spacing is set to 0.004 m, with 16 material points per rectangular element, resulting in a total of 20,200 material points. The parameters of the water include: the density of ρ_w=10^3 kg/m^3 and the viscosity of 1×10^{-3} Pa·s.

5.1.2. Model results

Fig. 7 compares the time history of the free surface profile from our MPM solver against SPH results [88] and PFEM data [89]. The MPM solution exhibits excellent agreement with both reference methods in capturing water surfaces at different time intervals (from $t = 0.05$ s to 0.18 s). This quantitative alignment verifies the fluid solver's capability to accurately model free-surface water. Crucially, the velocity fields (Fig. 7) demonstrate that our weakly compressible explicit MPM formulation resolves critical velocity features, with fidelity comparable to mesh-based PFEM and particle-based SPH approaches. This capability is essential for precise fluid-solid interaction force estimation in erosion modeling, where momentum transfer accuracy dictates sediment transport predictions.

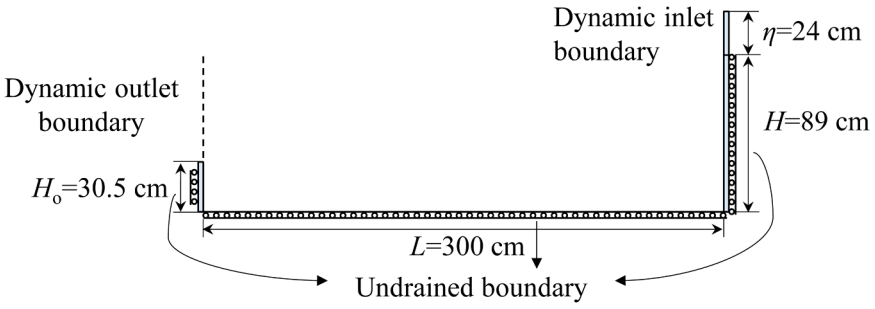

Fig. 8. The configuration of the water injection test.

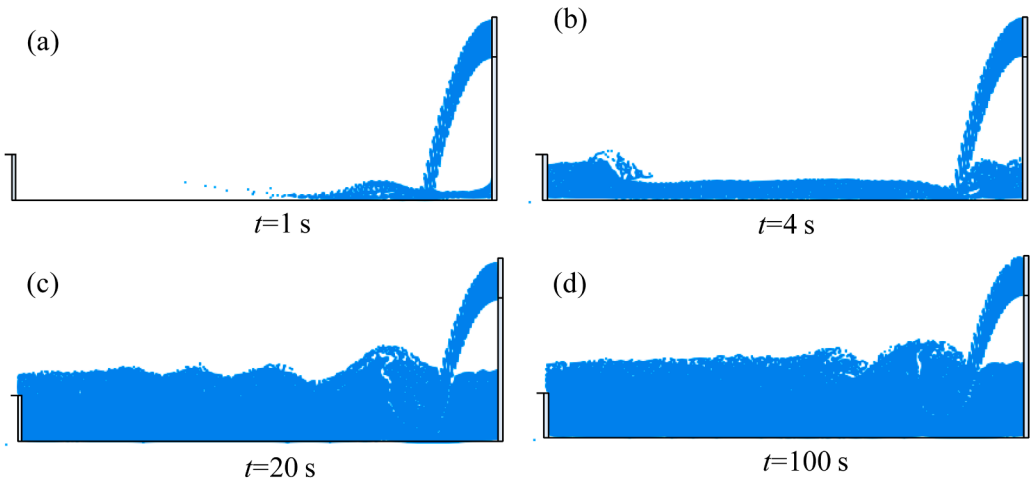

Fig. 9. The free surface of water in the injection test: (a) $t = 1$ s; (b) $t = 4$ s; (c) $t = 20$ s; (d) $t = 100$ s.

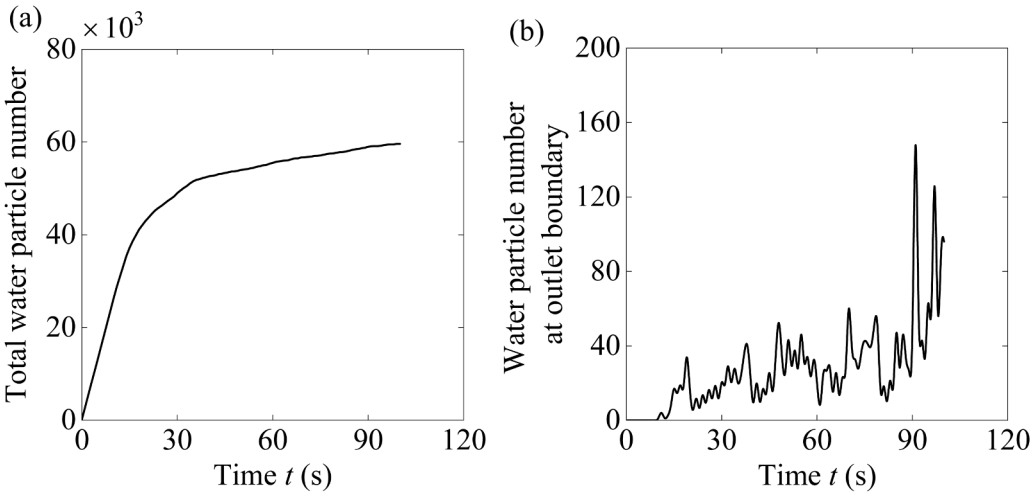

Fig. 10. Evolution of the number of total water particles and number of water particle number at the waiting zone during simulation. (a) The number of total water particles; (b) The number of water particle number at the waiting zone.

5.2. Example 2: water injection

5.2.1. Model description

The study further models the water injection process, in which water with a constant inflow velocity is injected into a water tank. This case is used to validate both the effectiveness and computational efficiency of the proposed boundary algorithm described in Section 4.3. As illustrated in Fig. 8, the irregularly shaped water tank has a length of 300 cm, with the heights at the left and right sides set to 30.5 cm and 89 cm, respectively. The height of the inlet boundary is set to 24 cm, and the inflow velocity is specified as 0.01 m/s. During the simulation, the time step is set to 1×10^{-4} s to ensure computational convergence, and the grid spacing is set to 0.01 m. The boundary conditions in the MPM model are implemented according to the proposed boundary algorithm in Section 4.3.

5.2.2. Model results

Fig. 9 presents the temporal evolution of the water injection process simulated using the MPM framework with our proposed boundary algorithm. Analysis focuses on the algorithmic performance of the proposed boundary treatment. As shown in Fig. 9, the results demonstrate that water particles are injected into the tank with a constant velocity. Once the water particles are beyond the water tank (i.e., the computational domain), the particles are moved and transferred into the waiting zone. This demonstrates the boundary scheme's effectiveness in adding and moving water particles during the simulation.

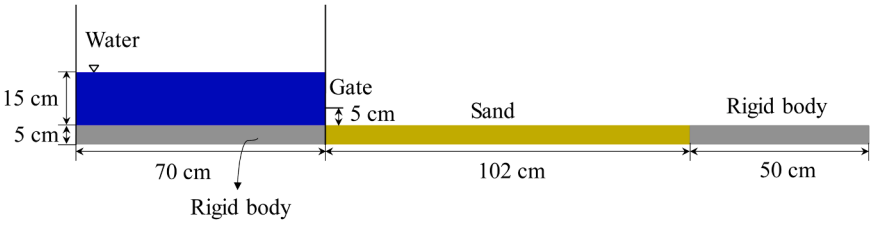

Fig. 11. Experimental setup for the wall-jet surface erosion.

Fig. 10 presents the temporal evolution of both the total number of water particles and the number of water particles in the waiting zone during the simulation. As shown in Fig. 10(a), the total number of water particles increases nonlinearly over time. The particle count rises rapidly during the initial stage. However, once the water reaches the outlet boundary, the rate of increase slows down. This is because some particles at the outlet boundary are transferred into the waiting zone, where they await reintroduction into the calculation. This behavior indicates that the proposed outflow boundary can effectively reduce the computational cost by decreasing the total number of water particles. Fig. 10(b) illustrates the number of water particles in the waiting zone throughout the simulation. At approximately $t = 10$ s, the water particles arrive at the outlet boundary, and some particles exit the computational domain and are transferred into the waiting zone. As time progresses, the number of particles in the waiting zone experiences fluctuations. These observations validate the effectiveness of the proposed boundary algorithm.

5.3. Example 3: wall-jet erosion

5.3.1. Model description

The third example is the wall-jet erosion, a small-scale and short-term surface erosion case in which a reservoir of water is suddenly released to erode an underlying sand bed. This benchmark mainly evaluates the performance of the proposed MPM framework in modeling the surface erosion by a detailed comparison between experimental observations and numerical predictions from both the present method and existing approaches.

Fig. 11 illustrates the prototype experimental setup for wall-jet erosion by Khanpour et al. [90]. In this experiment, a reservoir measuring 70 cm × 15 cm is filled with water and positioned atop a rigid base of 70 cm × 5 cm. At the lower left corner of the reservoir, a 5 cm-long gate is installed, which can be rotated to release the water. Upon opening the gate, a wall jet is released to erode a sand bed with dimensions of 102 cm × 5 cm. To the right of the sand bed, an additional rigid body measuring 50 cm × 5 cm is placed to close the model setup.

During the simulation, the basic geometry of the MPM model is the same as the experimental setup. The Eulerian grid is discretized with a spacing of 0.004 m, and each rectangular element contains 16 material points. In total, 104,300 material points are used to represent the soil-solid phase, while 51,000 material points are employed for the fluid phase. A small time-step dt=2.5 × 10^{-6} s is employed to satisfy the computational convergence.

According to Khanpour et al. [90], this wall-jet erosion case involves only bed-load transport, with nearly zero suspended-load particles observed. Therefore, only the parameters for the elastoplastic-$\mu(I)$ solid-fluid transition relation are required, as summarized in Table 2. Using the calibration method in Appendix B, we can obtain the model parameters. For the elastoplastic stress, the dimensionless referential elastic modulus E_0, Poisson's ratio ν, and constant controlling nonlinear stiffness n are set to 216, 0.2, and 0.5, respectively. The friction angle φ is reported as 35° [90]. Other parameters are based on typical values reported by Feng et al. [14]. For the viscous stress parameters, the sand

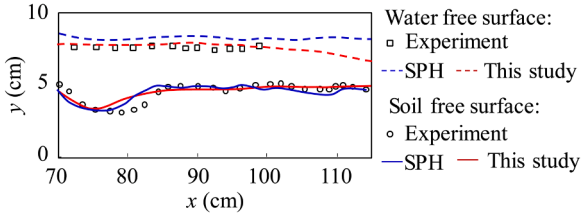

Fig. 13. Comparison of the final soil bed surface and water free surface from experimental data [90], MPM results in this study, and SPH results [90].

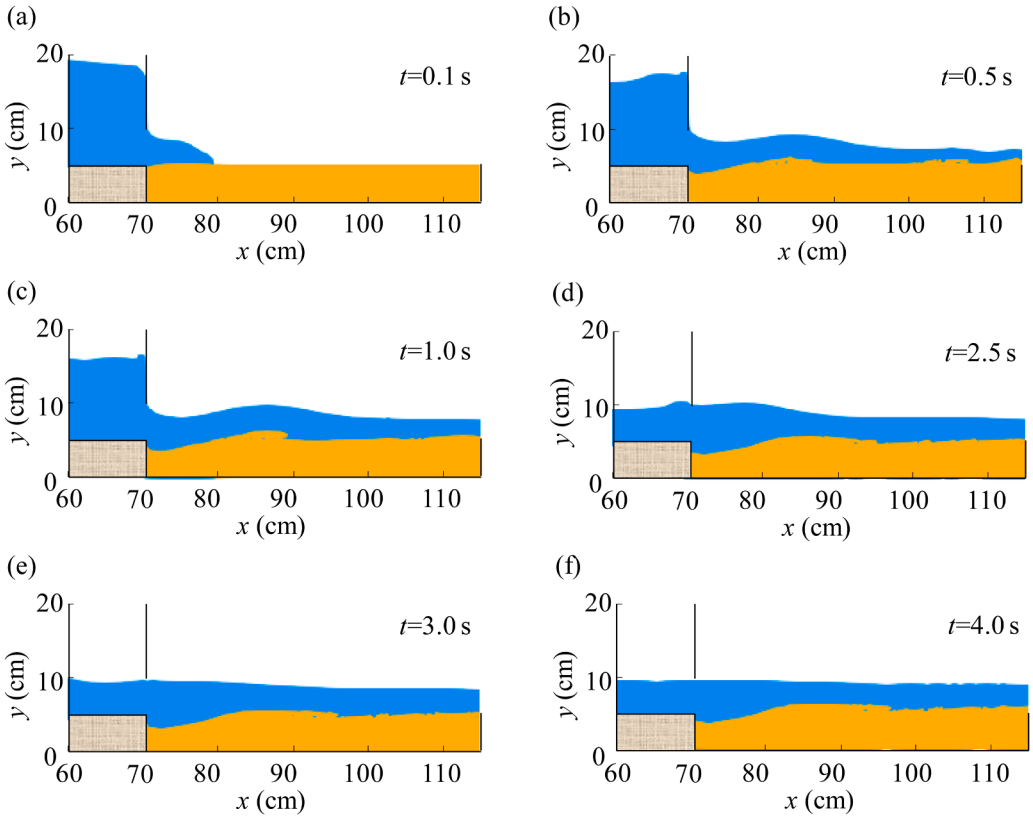

Fig. 12. The small-scale short-term wall-jet surface erosion process from the MPM simulation. (a) $t = 0.1$ s; (b) $t = 0.5$ s; (c) $t = 1.0$ s; (d) $t = 2.5$ s; (e) $t = 3.0$ s; (f) $t = 4.0$ s.

used in the study has the following properties: ρ_d=2650 kg/m^3 [90], static friction coefficient μ_s=tan (35°) =0.70, dynamic friction coefficient μ_d=0.770, and inertial number I_0=0.279. Additional material properties include the particle diameter d = 0.85 mm [90], random close volume fraction Φ_c=0.70, and dynamic loosening factor $\Delta\Phi$=0.29 [14]. For the water, the parameters used include: the density of ρ_w=10^3 kg/m^3 and the viscosity of 1 × 10^{-3} Pa·s.

5.3.2. Model results

Based on the two-phase two-point MPM model, the wall-jet erosion case is simulated. Fig. 12 illustrates the wall-jet-induced surface erosion process at various time intervals. At t = 0.1 s, immediately after the gate is opened, the water begins to erode the sand bed, and a scour hole starts to form as sand particles are taken away by the shear stress exerted by the water. Between t = 0.5 s and t = 1.0 s, the scour hole continues to deepen and expand. During this period, sand particles predominantly move along the bed, with virtually no particles entering the water as suspended-load transport. This observation confirms that the wall-jet erosion experiment, which has limited water velocity, primarily generates bed-load transport. From t = 2.5 s to t = 4.0 s, both the reservoir water level and the water velocity decrease. The size and shape of the scour hole remain unchanged during this interval, indicating that the maximum scour depth is reached at approximately t = 2.5 s. These simulation results are in good agreement with the findings reported by Khanpour et al. [90] and Nikeghbali et al. [91], demonstrating the effectiveness and reliability of the MPM approach.

Fig. 13 compares the final water's free surface and soil bed surface obtained from the MPM results in this study, experimental data [90], and SPH simulation results [90]. When comparing the final water free surface among these three sources, it is evident that the proposed MPM model provides results that are closer to the experimental data than those obtained from the SPH simulations. This demonstrates the effectiveness of the MPM approach in accurately capturing the water surface during the surface erosion process. Regarding the soil bed surface, both the SPH and MPM simulations are able to reproduce the erosion profile, particularly the maximum local scour depth, in good agreement with the experimental observations. These findings further validate the capability and reliability of the proposed MPM model for simulating surface erosion phenomena.

To further validate the proposed MPM model, the evolution of the relative scour depth S/S_{max} is compared among the results from the present MPM simulations, SPH results [90], and experimental data [90]. As shown in Fig. 14, the MPM results exhibit a closer agreement with the experimental data than the SPH simulations. While the differences between the SPH and MPM results may arise from various factors, the superior alignment of MPM with physical measurements underscores the efficacy of our elastoplastic-$\mu(I)$ phase-transition model in capturing bed-load transport during the surface erosion process.

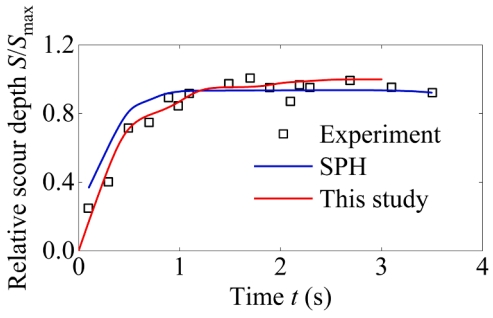

Fig. 14. Comparison of the relative scour depth from experimental data [90], simulation results from MPM in this study, and SPH results by [90].

5.4. Example 4: overtopping erosion

5.4.1. Model description

The third validation case is the overtopping erosion, which is commonly observed in dams where downstream flow progressively erodes the dam. The flume experiment of overtopping erosion by Schmocker [92] is employed herein for the benchmark. Distinct from previous benchmarks, this scenario simultaneously considers: (i) the boundary algorithm in Section 4.3; (ii) the two-phase two-layer MPM model in solving coupled fluid-sediment evolution; (iii) computational robustness across extended timescales (t > 20 s).

Fig. 15 shows the experimental setup for Test 52 in Schmocker [92]. The non-cohesive dam is constructed in a trapezoidal shape. The top base's length L_k of the trapezoidal dam is 0.10 m, and the dam height w is 0.2 m. The side slopes of the dam have an angle corresponding to tan θ=1:2. The water tank used in the experiment has a height of 0.7 m and a width of 8.0 m. During the test, a constant inflow discharge rate of Q_0=0.008 m^3/s is maintained. Given the tank width of 0.2 m, the unit-width discharge is 0.04 m^2/s. The distance between the inflow boundary and the dam is set at 1.0 m.

During the simulation, the basic geometry of the MPM model is the same as the experimental setup. The Eulerian grid is discretized with a spacing of 0.01 m, and each rectangular element contains 4 material points. The dynamic inflow boundary algorithm in Section 4.3 is employed to model the inflow with a horizontal velocity v_x=0.2 m/s, corresponding to the unit-width discharge of 0.04 m^2/s. A small time step dt=5 × 10^{-6} s is employed to satisfy the computational convergence. The total simulation time is 30 s. The no-slip condition is considered according to Zhou et al. [58].

Table 2 lists the parameters for this case. Since the experiments in this section and Section 5.3 utilize noncohesive sand, some fundamental parameters remain consistent. Key parameters are obtained from existing reported data: the friction angle φ is reported as 30° [58,60,92]. ρ_d=2650 kg/m^3 [58], static friction coefficient μ_s=tan (30°)=0.577, dynamic friction coefficient μ_d=0.660, and inertial number I_0=0.279. Additional material properties include the particle diameter d = 1 mm, random close volume fraction Φ_c=0.70, and dynamic loosening factor $\Delta\Phi$=0.29. For the water, the parameters used include: the density of ρ_w=10^3 kg/m^3 and the viscosity of 1 × 10^{-3} Pa·s.

5.4.2. Model results

We first present the overtopping erosion process simulated using the proposed MPM model, as illustrated in Fig. 16. Consistent with the experimental procedure described by Schmocker [92], the initial time (t = 0) is defined as the moment when the reservoir water level reaches the dam crest. At t = 2 s and t = 4 s, the flow begins to erode the downstream slope of the dam, while some soil particles on the upstream slope are also taken away by the reservoir water. As time progresses from t = 8 to t = 20 s, continuous water flow leads to further erosion of dam particles, resulting in a noticeable decrease in dam height. Simultaneously, the reservoir water level gradually drops during the overtopping process. By t = 30 s, the majority of the dam particles have been eroded, indicating that the dam has essentially failed. These qualitative observations of the overtopping erosion process from the MPM simulations are in good agreement with previous experimental and numerical studies [58,60,92], thereby demonstrating the effectiveness and reliability of the proposed MPM model.

We further quantitatively compare the evolution of the dam profile from the MPM simulation results with the experimental data reported by Schmocker [92], as shown in Fig. 17. Throughout the overtopping erosion process, from initiation to dam failure, the dam profiles predicted by the MPM model show good agreement with the experimental observations, demonstrating the model's capability to accurately capture the overtopping process.

Additionally, Fig. 17 presents the evolution of the velocity magnitude of soil particles. It is observed that, from the onset of overtopping to

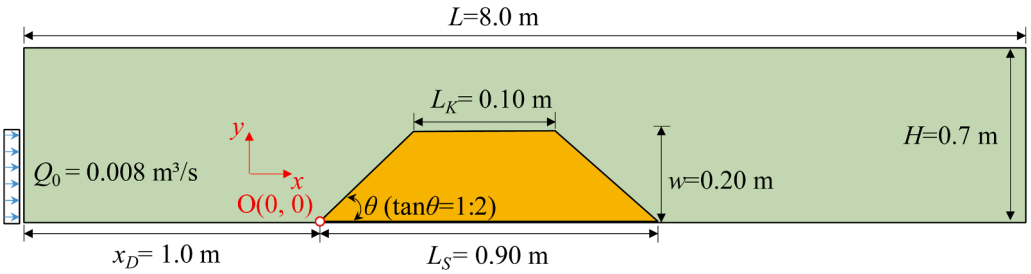

Fig. 15. Experimental setup for the small-scale long-term overtopping erosion.

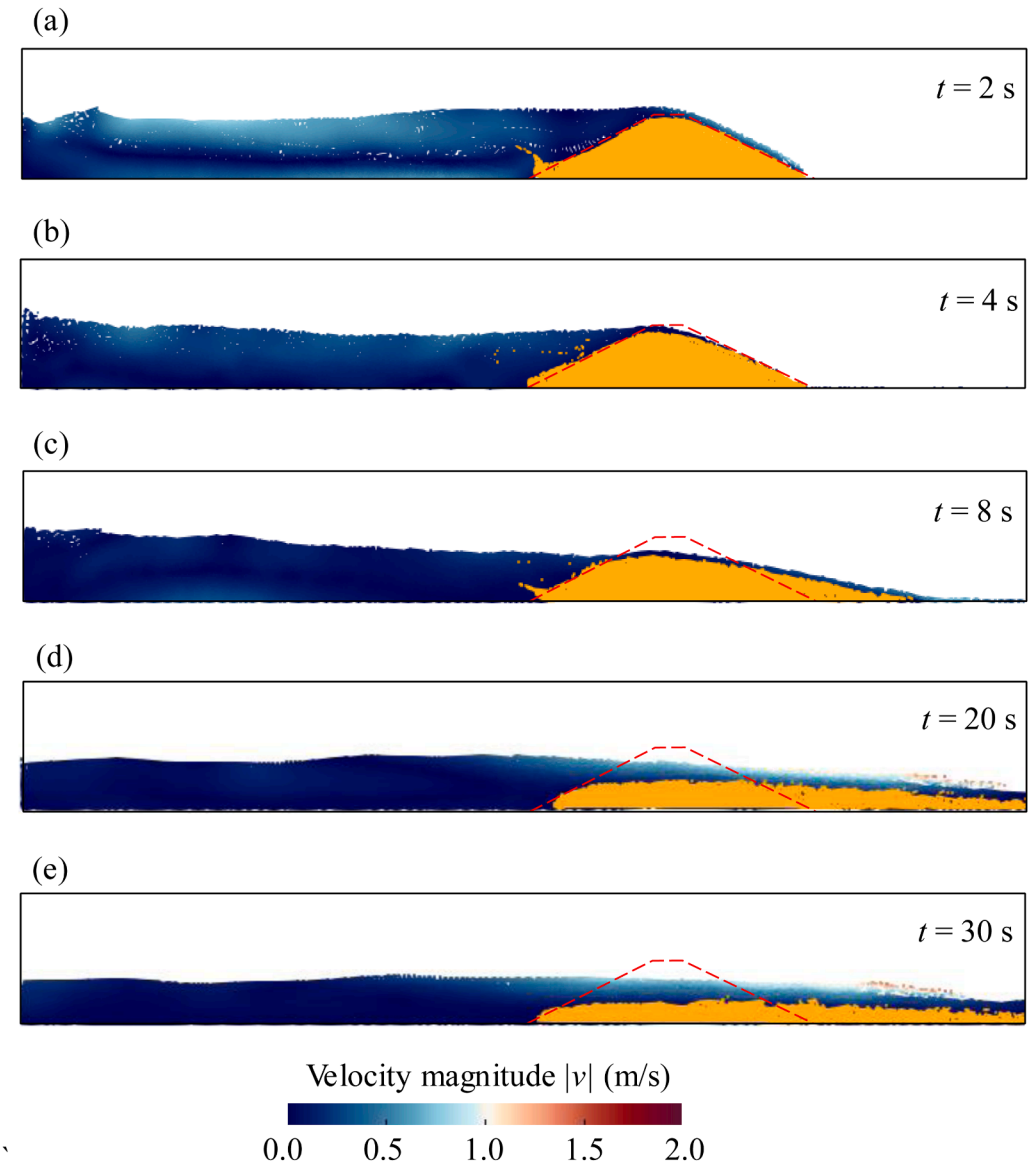

Fig. 16. The evolution of the fluid velocity during the overtopping erosion process using the proposed MPM-based surface erosion model. (a) $t = 2$ s; (b) $t = 4$ s; (c) $t = 8$ s; (d) $t = 20$ s; (e) $t = 30$ s.

dam failure, the velocity of soil particles at the surface is consistently higher than that of particles within the dam interior. The maximum particle velocity occurs between $t = 8$ s and $t = 10$ s, indicating that the fastest soil movement takes place at the surface during this period, rather than at the final failure stage.

5.5. Example 5: tsunami overflow erosion

5.5.1. Model description

The fifth validation case is the tsunami overflow erosion, in which the tsunami overflow generates the erosion process behind the vertical dike. The experiment test by Arikawa et al. [93] is employed to model the tsunami overflow erosion, which has a larger model size and a larger

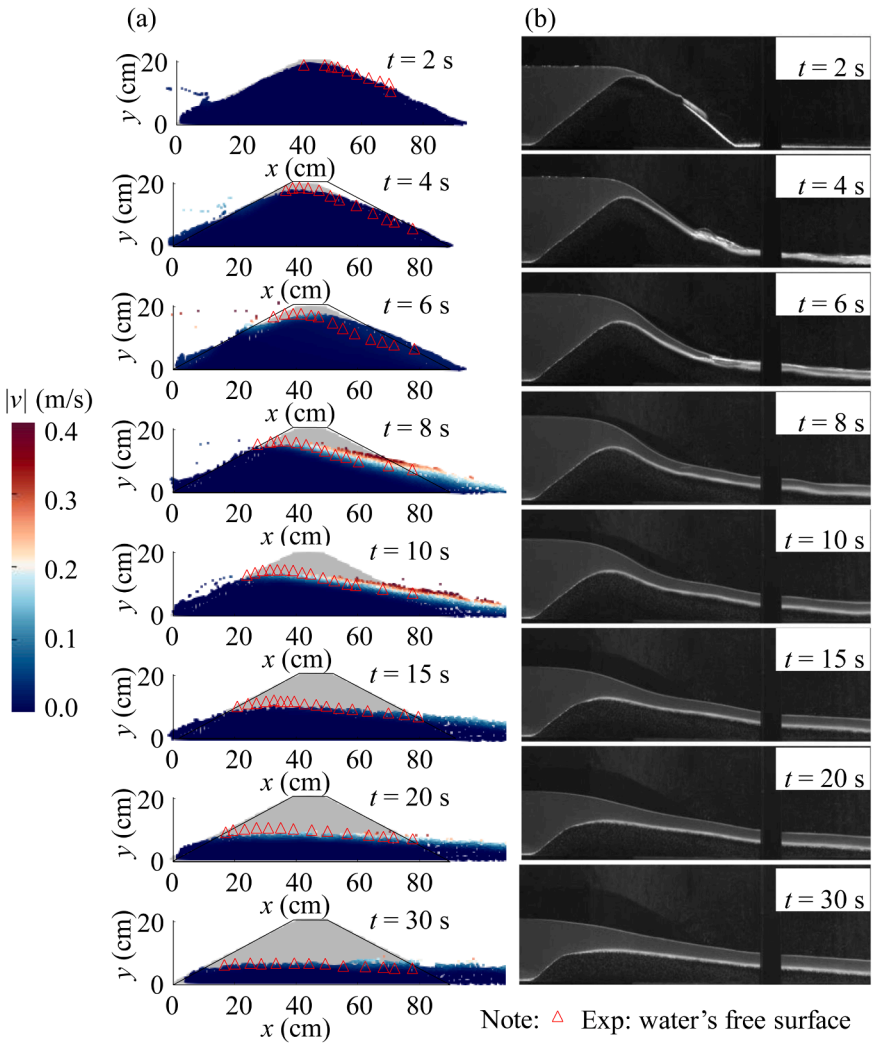

Fig. 17. Comparison of the dam profile between the MPM solution and experimental results [92] (where red triangle denotes the experiment results). (a) MPM results; (b) experimental results.

erosion time than previous cases. The experimental test for this case is simulated by methods such as SPH [57,94] and PFEM [54]. However, to the author's knowledge, no MPM model has been conducted for the tsunami overflow erosion.

Fig. 18(a) illustrates the experimental configuration for tsunami-induced surface erosion. A continuous water column over a vertical dike with initial height η and prescribed inlet velocity V_{in} is released to erode a sand bed of length L and height H. To maintain a consistent water level of $H + h$, a small elevation step of height h is incorporated at the downstream end of the sand bed. Upon water is released, a localized scour hole develops behind the dike due to tsunami overflow mechanisms.

Fig. 18(b) presents the MPM simulation setup for the tsunami overflow erosion scenario, replicating the experimental dimensions of Case 3 from Arikawa et al. [93]. This benchmark case was selected specifically because it documents scour hole evolution at multiple time intervals. The domain geometry, including sand bed height H, length L, and downstream elevation step h, is identical to the experimental configuration. The Eulerian grid is discretized with a spacing of 0.01 m, and each rectangular element contains four material points (i.e., the particle diameter is 0.025 m), resulting in a total of 78,130 soil solid particles. For the water phase, the inlet boundary (as described in Section 4.3) is used to generate the tsunami overflow with a constant velocity of 1.09 m/s. The dynamic outlet boundary algorithm (also detailed in SubSection 4.3) is applied to control the outflow of water particles from the computational domain. A small time step of dt=5 × 10^{-6} s is adopted to ensure computational stability and convergence. The total simulation time is set to 120 s. Since only a few soil parameters are reported by Arikawa et al. [93], most parameters in this case are adopted from the typical sand properties validated in previous sections (see Table 2).

5.5.2. Model results

Fig. 19 compares the tsunami overflow-induced erosion holes obtained from the proposed MPM-based surface erosion model with the experimental results reported by Arikawa et al. [93] at different time steps. As shown in Fig. 19(a) and Fig. 19(b), both the MPM simulation and the experimental test produce a large erosion hole adjacent to a smaller one. However, only quantitative data for the large hole are available from Arikawa et al. [93] and Wang et al. [57]. Therefore, we compare the experimental data for the large hole (indicated by circles) with the MPM results for the large hole (indicated by rectangles) in Fig. 19(a). The comparison demonstrates that the large scour hole predicted by the MPM model closely matches the experimental observations. These results indicate that the proposed MPM model is capable of accurately describing the tsunami-induced erosion process.

Fig. 20 further compares the evolution of scour depth from the MPM model in this study with experimental data [93] and PFEM results [54]. It is observed that the MPM results provide accurate predictions of scour

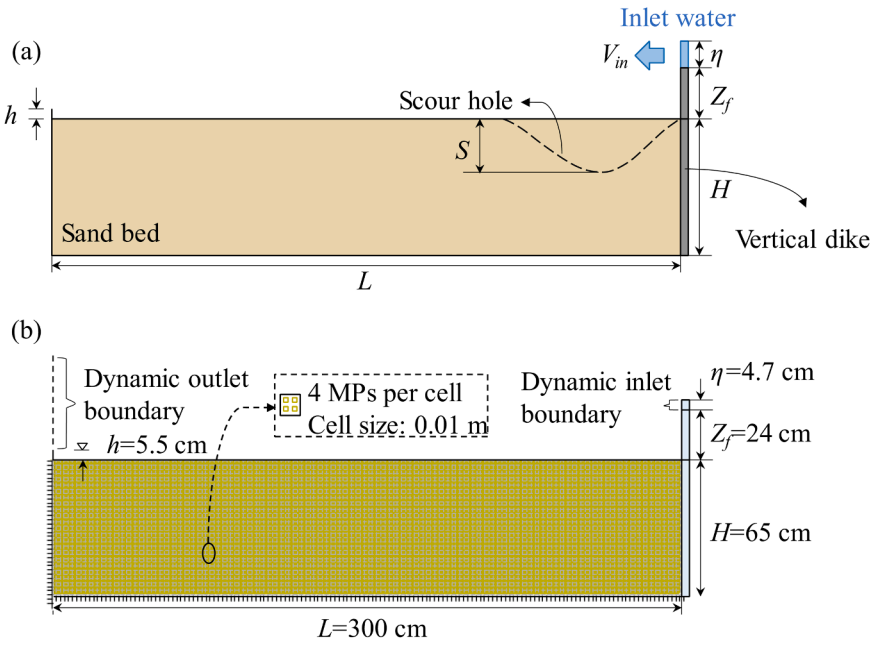

Fig. 18. Illustration of the surface erosion by tsunami overflow. (a) Experimental setup; (b) MPM setup.

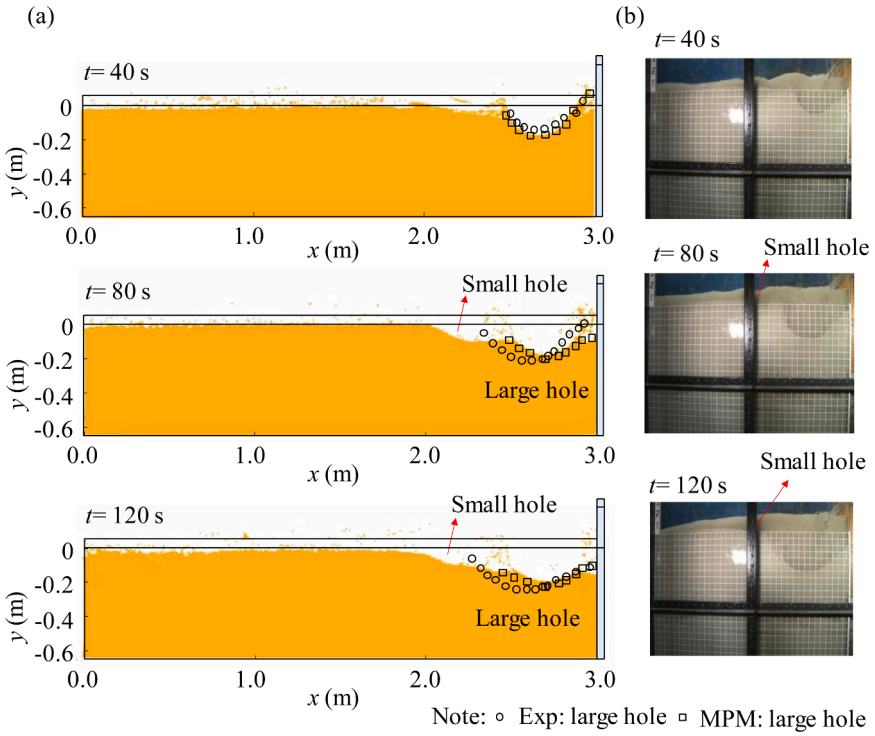

Fig. 19. Comparison of the tsunami overflow-induced erosion hole from proposed MPM-based surface erosion model and experimental results [93]. (a) MPM results; (b) Experimental results.

depth during the early stages of surface erosion. However, beyond $t = 60$ s, the model yields a slight underestimation that remains within acceptable limits. Notwithstanding this minor inconsistency, the developed MPM-based surface erosion model effectively captures the overall evolution of the scour hole.

Fig. 21 illustrates the temporal evolution of solid particle velocity magnitude during the erosion process. In the initial erosion phase (t = 10–20 s), a localized scour hole develops beneath the flow, with sediment transport exclusively limited to bed-load particles. The moving velocity of these bed-load particles is comparatively low in the whole process. As the process advances ($t = 40$–60 s), the fluid-solid interaction forces drive progressive enlargement of the scour hole, during which both bed-load and suspended-load transport regimes become evident. The suspended-load particles show a larger moving velocity than the bed-load particles. By the later stage (t = 80–120 s), the scour hole undergoes significant deepening and lateral expansion, resulting in the detachment and transport of particles beyond the computational domain. These observations indicate the proposed MPM model can

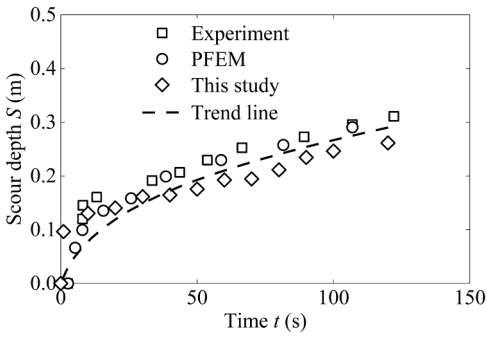

Fig. 20. Comparison of the scour depth from MPM-based surface erosion model, experiment [93], and PFEM [54].

effectively describe the movement of both bed-load and suspended-load particles.

Fig. 22 illustrates the temporal evolution of fluid velocity during the erosion process, which constitutes a primary driver for scour hole formation [57,94]. Throughout the simulation, the inflow velocity near the inlet boundary remains constant, consistent with experimental conditions and validating the effectiveness of the boundary algorithm. Furthermore, the MPM fluid solver successfully captures vortex generation, a key mechanism governing scour development. These vortices exhibit nonlinear temporal evolution, demonstrating greater intensity during initial erosion stages ($t < 60$ s) and progressively weakening as the scour hole forms and stabilizes. At $t = 40$ s and 80 s, two distinct vortices can be observed above the large and small scour holes, as shown in Fig. 22. This observation demonstrates that the proposed MPM model is capable of accurately capturing vortex generation and the associated formation of scour holes. However, it should be noted that, while the MPM model effectively represents vortex structures with a particle spacing of 0.025 m, the computational process is time-consuming, requiring approximately 30 h to complete. This limitation will be addressed in future work, and a more detailed discussion of this issue is provided in Section 6.

6. Discussion and analysis

Building upon the evaluation of the proposed MPM-based surface erosion model presented in the preceding section, we now focus on analyzing this new model. This analysis is conducted through comparative assessments in two primary aspects: (i) comparison with results from existing particle-based methods, and (ii) comparison with established empirical erosion criteria. Furthermore, limitations inherent to the proposed approach for modeling surface erosion are discussed, providing context for future research directions.

6.1. Comparing to existing particle methods

In this subsection, we compare our MPM results with those of other advanced Lagrangian particle methods, specifically the SPH-based surface erosion model [57] and the PFEM-based surface erosion model [54], using the tsunami overflow case presented in SubSection 5.5. Fig. 23 compares the bed surface evolution from the three methods. All three approaches successfully resolve the fluid-solid erosion interface due to the advantage of Lagrangian particle techniques. However, some differences exist: (i) Evolution of erosion surface: SPH and PFEM simulate surface erosion by converting solid-phase particles at the fluid-solid interface into fluid particles based on the Shields criterion, i.e., the solid particle deletion process, effectively modeling a decreasing erosion surface over time. Our MPM model uniquely achieves dynamic surface evolution through physics-driven solid-fluid coupling modeling. (ii) Bed-load and suspended-load representation: SPH/PFEM fail to resolve soil particle state at the bed-load and suspended-load, whereas our MPM model explicitly captures these via our state-dependent constitutive model.

The above differences highlight that the proposed MPM approach can accurately and simultaneously capture the evolution of the soil-fluid interface, as well as the dynamics of bed-load and suspended-load particles during surface erosion.

6.2. Comparing to empirical erosion criteria

Within continuum-based numerical models for surface erosion,

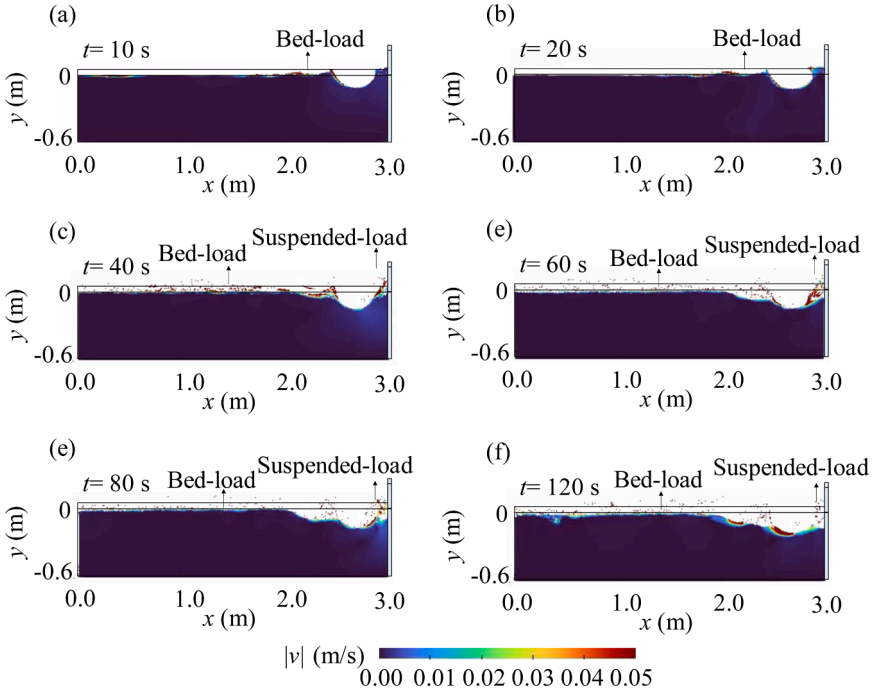

Fig. 21. The velocity magnitude of the solid phase at different time steps. (a) $t = 10$ s; (b) $t = 20$ s; (c) $t = 40$ s; (d) $t = 60$ s; (e) $t = 80$ s; (f) $t = 120$ s.

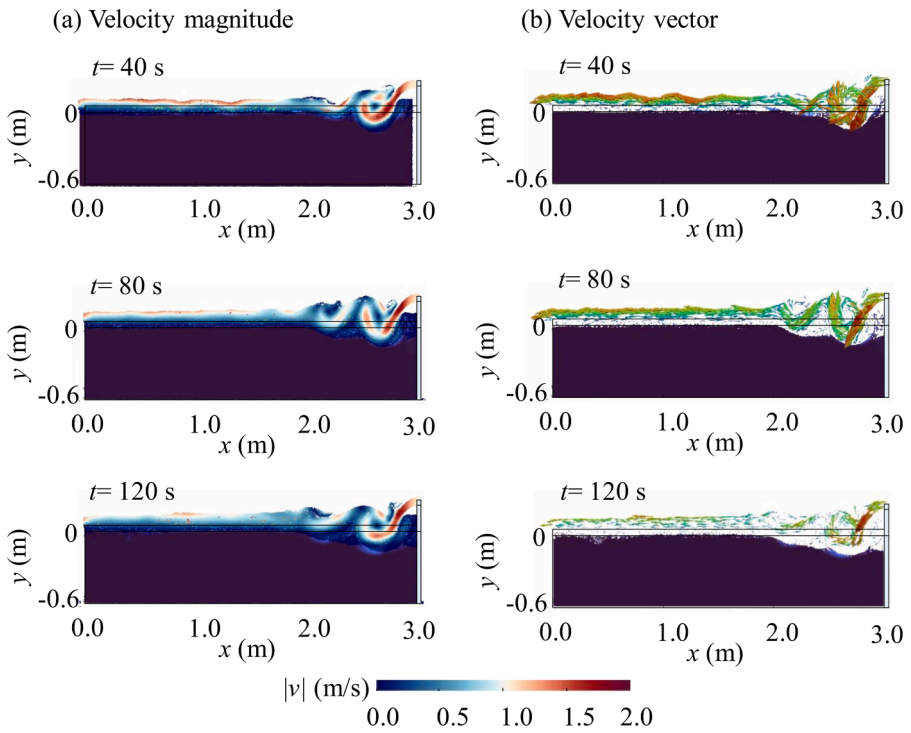

Fig. 22. The velocity field of the fluid phase at different time steps. (a) Velocity magnitude; (b) Velocity vector.

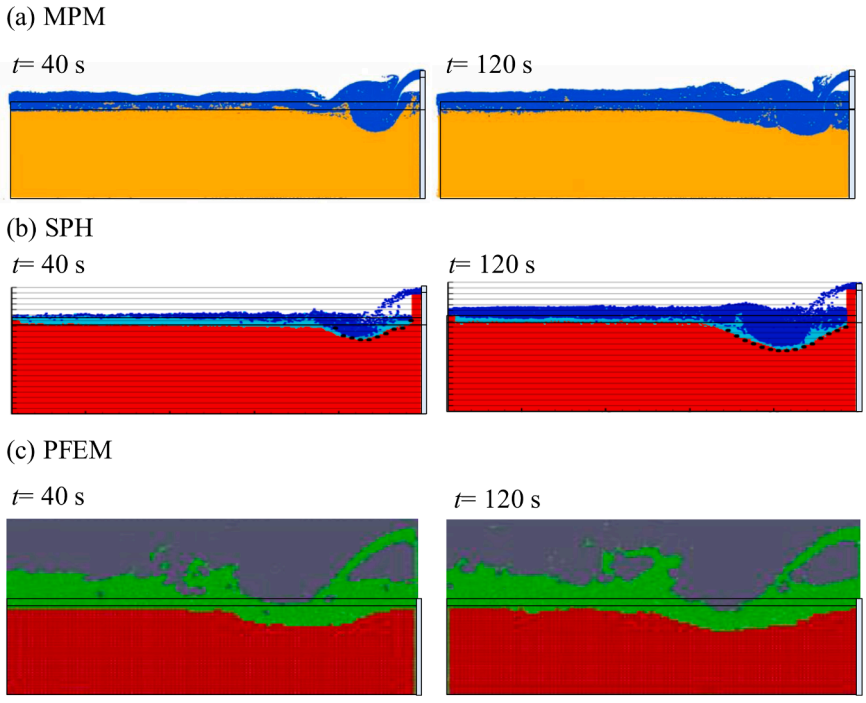

Fig. 23. Comparison of the soil bed surface from SPH results [93], simulation results from MPM in this study, and PFEM results [54]. (a) MPM results; (b) SPH results; (c) PFEM results.

conventional approaches typically solve the Navier-Stokes equations for fluid dynamics while approximating sediment transport via empirical formulae to update the bed surface. This methodology is implemented in both Lagrangian particle methods (e.g., [54,55,57]) and Eulerian mesh-based frameworks (e.g., [37–39]). Critically, these models rely on empirical erosion criteria to initiate sediment motion, inherently limiting their applicability to specific hydraulic and sedimentary conditions. In contrast, the proposed model simulates surface erosion without empirical erosion criteria. Given that both approaches ultimately model the same physical phenomenon, the MPM results should inherently reflect the underlying initiation mechanism of surface erosion. To validate this point and demonstrate the model's robustness, we further compare MPM simulation results against established empirical erosion criteria.

The initiation of surface erosion refers to the onset of soil particle movement. In the existing literature, most studies employ the Shields number, which is related to shear stress and shear velocity, to characterize the initiation of particle movement. The Shields number is expressed as follows:

$$\tau_{cr} = \rho_w u_{cr}^2 \tag{57}$$

$$\theta_{cr} = \frac{\tau_{cr}}{\rho_w g(G_s - 1)d} \tag{58}$$

where τ_{cr} is the critical shear stress; u_{cr} is the critical shear velocity; θ_{cr} is the Shields number, G_s is the specific gravity.

Building upon this foundation, numerous studies have employed critical shear stress, critical shear velocity, and the Shields number to characterize erosion thresholds through experimental testing, field observations, and theoretical analysis. This extensive research has subsequently yielded many empirical erosion criteria. For reference and comparative analysis, three representative initiation criteria are presented below:

- Erosion criterion from Shields [17] is expressed as follows:

$$\tau_{cr} = 0.63 d_{50} \tag{59}$$

$$u_{cr} = (\tau_{cr}/\rho_w)^{0.5} \tag{60}$$

where d_{50} is particle diameter, with the unit of mm, and the unit of τ_{cr} is Pa.

- Erosion criterion from Rijn [95] is expressed as follows:

$$d_* = d_{50}\left(\frac{\rho' g}{\nu^2}\right)^{1/3}, \rho' = G_s - 1 \tag{61}$$

$$\theta_{cr} = \begin{cases} 0.24 d_*^{-1}, 1 < d_* \le 4 \\ 0.14 d_*^{-0.64}, 4 < d_* \le 10 \\ 0.04 d_*^{-0.1}, 10 < d_* \le 20 \\ 0.013 d_*^{-0.29}, 20 < d_* \le 150 \\ 0.055, 150 < d_* \end{cases} \tag{62}$$

$$u_{cr} = [\theta_{cr} g(G_s - 1) d_{50}]^{0.5} \tag{63}$$

where G_s is the specific gravity.

- Erosion criterion from Annandale [96], is expressed as follows:

$$\tau_{cr} = \frac{2}{3}\gamma_w d(G_s - 1)\tan\varphi \tag{64}$$

$$u_{cr} = (\tau_{cr}/\rho_w)^{0.5} \tag{65}$$

Table 4
The empirical initiation velocity in this study.

Parameter	Example 3	Example 4	Example 5
Specific gravity G_s	2.65	2.65	2.65
Particle diameter d_{50} (m)	$0.85\bullet10^{-3}$	$1\bullet10^{-3}$	$2\bullet10^{-3}$
Friction angle φ (°)	35	30	30
Critical velocity (Shields's model) (m/s)	0.0079	0.0079	0.0079
Critical velocity (Rijin's model) (m/s)	0.0079	0.0081	0.0092
Critical velocity (Annandale's model) (m/s)	0.0003	0.0003	0.0006

Utilizing the three aforementioned erosion initiation models, critical shear velocities for the surface erosion cases (Examples 3–5) are determined and presented in Table 4.

To validate the MPM results against these theoretical thresholds, horizontal velocity profiles are extracted from simulations (see Fig. 24). During the initial stage of surface erosion (see Fig. 24(a1), (b1), and (c1)), the maximum horizontal velocities align closely with the critical shear velocities, suggesting that the MPM framework inherently captures fundamental erosion initiation mechanics without empirical prescription. Given that mobilized particles may transiently exceed this threshold early in the erosion process, the peak horizontal velocity within each profile is interpreted as the effective critical shear velocity to maintain consistency. This approach enables spatial identification of erosion zones by correlating regions attaining critical velocities with observed particle mobilization. As illustrated in Fig. 24, zones reaching critical shear velocities correspond precisely to areas of active erosion (see Fig. 24(a2), (b2), and (c2)). Conversely, nearly all particles outside eroded regions fail to attain the critical shear velocity and remain stable. This agreement confirms the MPM model's ability to accurately simulate erosion initiation physics without empirical calibration, indicating that the proposed MPM model can serve as a practical alternative to empirical formula-based surface erosion simulation solvers.

6.3. Advantages of this model

Based on the above discussion, the proposed MPM model has shown the following advantages:

(i) **Description of soil-water interfaces**: Unlike traditional Eulerian-method-based surface erosion models (e.g., FVM), which require specialized techniques (e.g., level set or volume of fluid) to track surfaces, this work employs a Lagrangian description for both soil and water. This approach naturally and accurately captures the water's free surface and the soil-water interface without additional numerical treatment.

(ii) **Representation of erosion process**: Unlike existing Lagrangian-based surface erosion methods that rely on the non-physical deletion of solid particles with empirical relationships, this study provides a more physically consistent description by explicitly resolving the fundamental soil-fluid interactions.

(iii) **Representation of bed-load and suspended-load particles**: Unlike existing surface erosion methods, this work accurately captures both transport modes, bed-load and suspended-load, through a state-dependent formulation, without resorting to non-physical assumptions or processes.

(iv) **Mechanistic evaluation of erosion criteria**: Lastly, it is important to emphasize that this model itself serves as an effective tool for analyzing erosion initiation criteria (see Section 6.2). This represents a significant advance over the application of predetermined empirical criteria, providing a more fundamental, mechanics-based approach to the analysis of soil surface erosion.

6.4. Limitations and future works

Despite the advancements, four points must be addressed to enhance the accuracy of the proposed MPM model in future research:

(i) **Consideration of turbulent flow.** This study employs direct numerical simulation (DNS) of the Navier-Stokes equations, which effectively captures fluid behavior at low flow velocities. However, when extending the existing MPM fluid solver to model surface erosion for high-Reynolds number flows, it becomes necessary to incorporate a Reynolds-Averaged Navier-Stokes (RANS) model with an appropriate turbulence closure.

(ii) **Consideration of implicit time integration.** The present work employs an explicit two-phase two-point integration algorithm,

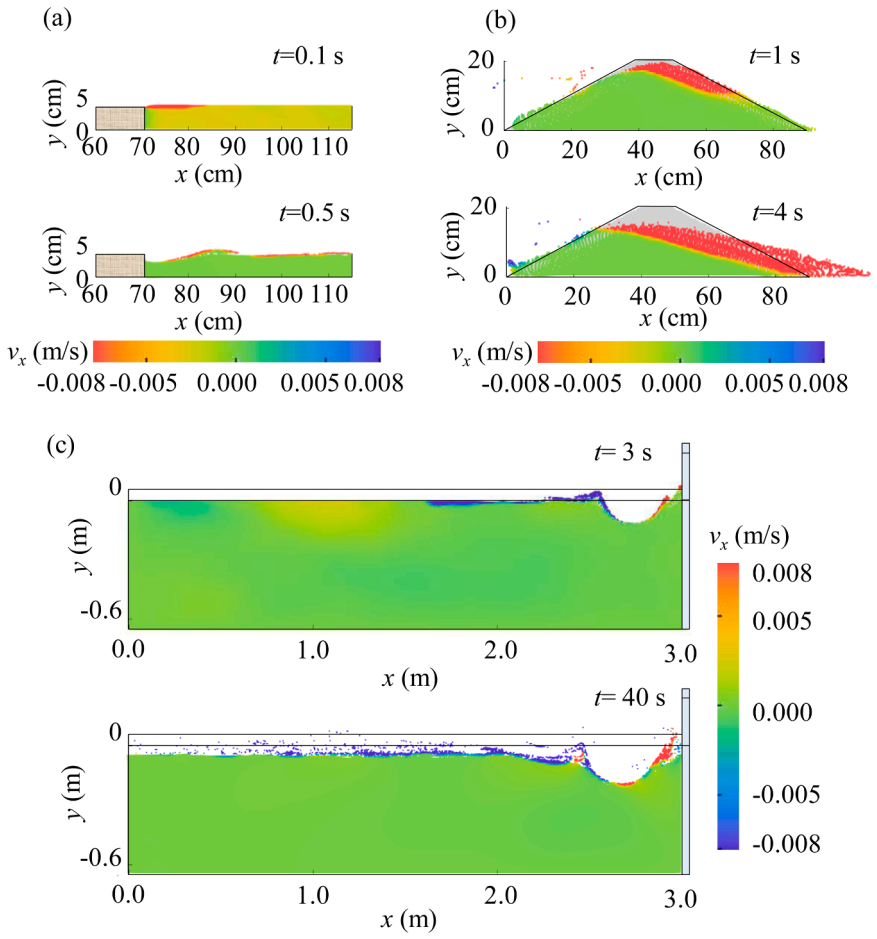

Fig. 24. The horizontal velocity profile of Example 3, 4, and 5 from MPM simulation. (a) Example 3: Wall-jet erosion; (b) Example 4: Overtopping erosion; (c) Example 5: Tsunami overflow erosion.

which has two limitations: (1) the explicit MPM scheme for the fluid phase might introduce non-physical pressure oscillations; (2) the explicit integration necessitates a small time step to satisfy the Courant-Friedrichs-Lewy (CFL) stability condition (see Appendix C). As a result, simulating long-duration erosion events incurs a high computational cost. For example, simulating the Tsunami overflow erosion in Section 5.5 requires approximately 30 h. To address the above limitations, future research should focus on developing an implicit MPM simulation, particularly for the fluid solver, that enables a stable pressure field with larger time steps. Such advancements are essential for efficiently modeling engineering-scale erosion processes.

(iii) **Consideration of fluid-structure-soil interaction.** The current work focuses on surface erosion without obstructing structures, which represent typical fluid-soil interaction problems. However, another important category of surface erosion involves the presence of obstructing structures, resulting in fluid-soil-structure interaction. This scenario is inherently more complex due to the need to account for both fluid-structure and soil-structure interactions. Future research should therefore aim to extend the present model to simulate these more complex fluid-soil-structure interaction problems.

(iv) **Consideration of three-dimensional simulation**. The current work focuses on developing an MPM model for soil surface erosion, with all simulations conducted in a two-dimensional framework. Future work should extend this model to three dimensions and apply it to large-scale, real-world engineering problems. To achieve this goal, the existing codebase must be extended to three dimensions, and GPU-accelerated computing should be implemented to manage the significantly higher computational demands of 3D simulations.

7. Conclusion

This study has proposed a novel MPM-based model for surface erosion modeling to address limitations in existing Lagrangian particle modeling methods. Our proposed MPM-based surface erosion model is established on the explicit two-phase two-point MPM algorithm, which can effectively resolve soil-fluid interactions during erosion processes. During the two-phase two-point MPM scheme, we developed the inflow/outflow boundary algorithm, which enables the addition and deletion of water particles at the boundaries to achieve accurate and efficient fluid boundary modeling within the MPM framework. We have also developed a state-dependent constitutive framework for soil solid, which is a piecewise constitutive relation including an elastoplasticity-$\mu(I)$ solid-to-fluid transition constitutive relation and an equation of state. The solid-fluid phase transition model captures the behavior of bed-load soil particles, while the equation of state describes the suspended-load regime.

The effectiveness of the proposed MPM framework is demonstrated through comprehensive validation against five distinct benchmark problems: dam break, water injection, wall-jet erosion, overtopping erosion, and tsunami overflow erosion. Across these cases, the MPM predictions show good agreement with experimental measurements and with results from other numerical models, indicating that the proposed framework can accurately reproduce the key features of soil surface

erosion under a wide range of hydraulic conditions.

In contrast to existing Lagrangian particle methods that typically rely on particle deletion and are unable to distinguish between bed-load and suspended-load regimes, the present MPM formulation achieves dynamic surface evolution through physics-based solid-fluid coupling. This allows for a more realistic and comprehensive representation of surface erosion without resorting to empirical erosion laws to drive material removal. When compared to conventional empirical erosion formulations, the proposed model predicts a similar critical initiation velocity, confirming that the physics-based coupling embedded in the MPM framework can effectively capture the mechanics of erosion onset. Consequently, the method provides a practical and reliable alternative to empirical formula-based approaches for simulating surface erosion in engineering applications.

Lastly, it should be emphasized that the numerical framework presented in this study can also be adapted to other continuum-based Lagrangian particle methods, such as SPH, PFEM, and MPS, to achieve a robust surface erosion simulation across different numerical platforms.

Data availability statement

The datasets generated during and/or analyzed during the current study are available from the corresponding author on reasonable request.

CRediT authorship contribution statement

Hang Feng: Writing – review & editing, Writing – original draft, Validation, Methodology, Investigation, Formal analysis, Conceptualization. **Zhen-Yu Yin:** Writing – review & editing, Supervision, Methodology, Funding acquisition, Conceptualization.

Declaration of competing interest

The authors declare that they have no known competing financial interests or personal relationships that could have appeared to influence the work reported in this paper.

Acknowledgments

This research is financially supported by the Research Grants Council (RGC) of Hong Kong Special Administrative Region Government (HKSARG) of China (Grant No.: T22-607/24-N, 15226322, 15229223, 15232224), and by the State Key Laboratory of Climate Resilience for Coastal Cities at the Hong Kong Polytechnic University.

Appendix A. Elastoplastic-$\mu(I)$ solid-fluid phase transition model

A1. Solid-like part

The frictional stress part in the phase transition model (see [14]) is described using the theory of elastoplasticity. Accordingly, the strain increment is divided into an elastic part $\delta\boldsymbol{\varepsilon}^e$and a plastic part $\delta\boldsymbol{\varepsilon}^p$:

$$\delta\boldsymbol{\varepsilon} = \delta\boldsymbol{\varepsilon}^e + \delta\boldsymbol{\varepsilon}^p \tag{A1}$$

The elastic strain increment can be employed to obtain the stress increment via $\delta\boldsymbol{\sigma}_f = \mathbf{K}_f{:}\delta\boldsymbol{\varepsilon}^e$, in which $\mathbf{K}_f$ is a fourth-order stiffness tensor, is determined by the elastic modulus E_f and Poisson's ratio ν. The elastic modulus E_f is established by considering the nonlinear characteristics of granular media, expressed as:

$$E_f = E_0 p_{at} \frac{(2.97-e)^2}{(1+e)} \left(\frac{p_f}{p_{at}}\right)^n \tag{A2}$$

where p_{at} is the atmospheric pressure (i.e., p_{at} =101.3 kPa); n is the Elastic constant controlling nonlinear stiffness; p_f is the hydrostatic part of frictional stress; e is the void ratio.

The yield function f_f is expressed as:

$$f_f = \frac{q_f}{p_f} - H_f \tag{A3}$$

where q_f is the deviatoric part of frictional stress; H_f is the hardening parameter, as follows:

$$H_f = \frac{M_p \varepsilon_d^p}{k_p + \varepsilon_d^p} \tag{A4}$$

where M_p is the slope of the failure line in the p_f-q_f plane, which is expressed as M_p= 6sinϕ_c/(3-sinϕ_c) (where ϕ_c is the friction angle) in triaxial compression condition (Lode angle effect is introduced to follow the Mohr-Coulomb criterion). ε_d^p is the plastic deviatoric strain. k_p is a constant controlling the plastic hardening behavior.

The flow rule is developed to consider the stress dilatancy (contraction or dilation), expressed in explicit form:

$$\frac{\partial g}{\partial p_f} = A_d \left(M_{pt} - \frac{q_f}{p_f}\right), \frac{\partial g}{\partial q_f} = 1 \tag{A5}$$

where A_d is a parameter controlling the magnitude of the stress-dilatancy; M_{pt} is the transformation stress ratio corresponding to the transitional state between a contractive and a dilatant behavior. If the current stress ratio is smaller than M_{pt}, the material is contractive. Otherwise, it is dilative.

The critical state concept is incorporated into the frictional stress model by considering the critical void ratio, which is expressed as:

$$e_c = e_{\text{ref}} \exp\left[-\lambda \left(\frac{p_f}{p_{at}} \right)^{\xi} \right] \tag{A6}$$

where e_{ref} is the initial critical-state void ratio; λ is the slope of the critical state line (CSL) in the e-log p_f plane; parameter ξ controls the nonlinearity of CSL.

The critical-state theory is implemented in the frictional stress model by modifying the peak stress ratio M_p and phase transformation stress ratio M_{pt} via $M_p = 6\sin\phi_p/(3-\sin\phi_p)$ and $M_{pt} = 6\sin\phi_{pt}/(3-\sin\phi_{pt})$, respectively. The peak friction angle ϕ_p and transformation angle ϕ_{pt} are expressed as:

$$\phi_p = \arctan\left[\left(\frac{e_c}{e} \right)^{n_p} \tan\phi_c \right] \tag{A7}$$

$$\phi_{pt} = \arctan\left[\left(\frac{e}{e_c} \right)^{n_d} \tan\phi_c \right] \tag{A8}$$

where n_p and n_d are parameters controlling the effect of particle interlocking.

A2: Fluid-like part

The unified elastoplastic-$\mu(I)$ model [14] employs a $\mu(I)$-based relation to describe the fluid-like stress, expressed as:

$$\dot{\sigma}_v = f_\Phi (2\mu|\dot{\gamma}|\ddot{\mathbf{e}} - \dot{\mathbf{e}}\ddot{\mathbf{e}} - \ddot{\mathbf{e}}\dot{\mathbf{e}}) \tag{A9}$$

where f_Φ is the volume fraction function, defined in Eq. (A10); μ is the friction coefficient, described by the $\mu(I)$ relation in Eq. (A11); $\dot{\mathbf{e}}$ is the deviatoric part of the strain rate tensor; $\ddot{\mathbf{e}}$ is the deviatoric part of the strain acceleration tensor; $|\dot{\boldsymbol{\gamma}}|$ is the second invariant of the deviatoric strain rate tensor, expressed as $|\dot{\boldsymbol{\gamma}}| = \sqrt{\dot{\mathbf{e}} : \dot{\mathbf{e}}/2}$.

$$f_\Phi = \rho_s \left(2d \frac{\Delta\Phi}{\Phi_c - \Phi} \right)^2 \tag{A10}$$

$$\mu(I) = \mu_s + \frac{\mu_d - \mu_s}{I_0 + I} I \tag{A11}$$

where ρ_s is the particle density; d is the particle diameter; $\Delta\Phi$ and Φ_c are the fluid-like coefficients; Φ is the volume fraction.

Appendix B. Calibration process of model parameters

The calibration process of the constitutive parameters in the elastoplasticity-$\mu(I)$ model is discussed in this section. A total of 19 parameters are required, which can be divided into two categories: those for the elastoplasticity-based frictional stress model and those for the $\mu(I)$-based viscous stress model. The standard calibration process involves obtaining the model parameters from laboratory tests, such as the triaxial test, isotropic compression test, and simple shear test. The detailed calibration process is described as follows:

(i) **Determination of elastic parameters of E_0, ν, and n:** Parameter ν can be obtained through data from triaxial tests by plotting the axial strain versus radial strain and determining ν from the slope of the line. Parameters E_0 and n can be obtained from isotropic compression tests.
(ii) **Determination of CSL parameters of e_{ref}, λ, and ξ:** To determine the parameters of e_{ref}, λ, and ξ, triaxial tests are conducted to obtain the CSL. In the CSL, the parameter e_{ref} is the reference void ratio corresponding to the mean effective frictional stress is zero; the parameter λ controls the slope of the CSL; the parameter ξ controls the position of the inflection point in the CSL.
(iii) **Determination of parameters φ_c and e_0:** Critical angle φ_c can take the value from the drained direct shear test or drained triaxial test. Parameter e_0 is the initial void ratio provided by the triaxial test.
(iv) **Determination of parameters A_d, k_p, n_p, and n_d:** These four parameters can be derived from undrained or drained triaxial tests.
(v) **Determination of parameters of ρ_s, d, and μ_s:** Parameter ρ_s and d can be determined via the laboratory test. Parameter μ_s takes the value of $\tan\varphi_c$.
(vi) **Determination of parameters of elastic parameters I_0, μ_d, Φ_c, and $\Delta\Phi$:** DEM simulation, undrained simple shear test, or the annular shear test, can be employed to obtain the $\mu(I)$ relation, further obtaining the μ_d and I_0. The stress-shear rate relation in the undrained simple shear test can be employed to obtain Φ_c and $\Delta\Phi$.

However, accurately determining the values of these parameters is challenging. Accordingly, typical values for sands can be used. These values, obtained from our previous study [14], are presented in Table A1.

Table A1
Calibration process of the parameter in the proposed unified elastoplasticity-$\mu(I)$ model.

Stress type	Parameter	Definition	Typical value regime	Standard calibration
Elastoplastic stress	E_0	Dimensionless elastic modulus	-	Isotropic compression test
	ν	Poisson's ratio	0.2–0.25	Triaxial tests
	n	Constant controlling elastic stiffness	0.5–0.7	Isotropic compression test
	φ_c	Critical-state friction angle	-	Drained direct shear test or drained triaxial test
	e_0	Initial void ratio	-	Triaxial test

(*continued on next page*)

Table A1 (*continued*)

Stress type	Parameter	Definition	Typical value regime	Standard calibration
	e_{ref}	Initial critical-state void ratio	-	Triaxial test
	λ	Constant controlling CSL nonlinearity	-	Triaxial test
	ξ	Constant controlling CSL nonlinearity	-	Triaxial test
	A_d	Constant controlling stress dilatancy	0.5–1.5	Undrained or drained triaxial test
	k_p	Plastic modulus–related constant	0.0001–0.01	Undrained or drained triaxial test
	n_p	Peak strength parameter	-	Undrained or drained triaxial test
	n_d	Phase transformation parameter	-	Undrained or drained triaxial test
Viscous stress	I_0	Referential inertial ratio	0.28	Undrained simple shear test, or the annular shear test
	ρ_s	Particle density (kg/m^3)	-	
	d	Particle diameter (m)	-	
	μ_s	Static friction coefficient (tanφ)	-	
	μ_d	Dynamic friction coefficient	-	
	Φ_c	Random close volume fraction	-	
	$\Delta\Phi$	Dynamic loosening factor	-	

Appendix C. Critical time step in explicit two-phase two-point MPM

Due to the fully explicit algorithm employed in this study, an effective time step is required. There are two approaches to determine a rational time step: (i) calculating the critical time step using theoretical formulas, which is necessary to satisfy the stability condition; and (ii) obtaining the critical time step through trial and error. In this section, we primarily discuss the former approach.

Since this study employs the explicit two-phase two-point MPM, the critical time step must satisfy both the Courant-Friedrichs-Lewy (CFL) condition and the stability criterion related to permeability. Accordingly, the critical time step is calculated using the following equation:

$$\Delta t_{cr} = \min\left(\Delta t_{cr}^{CFL}, \Delta t_{cr}^{k}\right) \tag{C1}$$

where Δt_{cr}^{CFL} is the CFL critical time step; Δt_{cr}^{k} is the permeability critical time step.

The CFL critical time step can be written as:

$$\Delta t_{cr}^{CFL} = \frac{\Delta h_e}{c} \tag{C2}$$

where Δh_e is the grid size; c is the compressional wave velocity traveling in a medium.

For the explicit algorithm related solely to the solid phase, the wave velocity is defined as:

$$c = \sqrt{\frac{K_s + 4G/3}{\rho_s}} \tag{C3}$$

where K_s and G are the bulk and shear modulus of the soil-solid part, respectively.

For the explicit algorithm related solely to the water, the wave velocity is defined as:

$$c = \sqrt{\frac{K_w}{\rho}} \tag{C4}$$

where K_w is the bulk modulus of the water.

For the explicit algorithm related to the saturated medium, the wave velocity is defined by Eq. (C5). We calculate the CFL critical time step by this equation.

$$c = \sqrt{\frac{\left(\frac{n}{K_w} + \frac{1-n}{K_s}\right)^{-1} + \frac{4}{3}G}{(1-n)\rho_s + n\rho_w}} \tag{C5}$$

The permeability critical time step can be defined as:

$$\Delta t_{cr}^{k} = \frac{-\frac{\rho_w g}{\rho_m k_w} + \sqrt{\left(\frac{\rho_w g}{\rho_m k_w}\right)^2 + 4\omega^2}}{\omega^2} \tag{C6}$$

$$\omega^2 = \frac{4E_s}{\rho_m (\Delta h_e)^2} \tag{C7}$$

$$\rho_m = \rho + \left(\frac{1}{n} - 2\right)\rho_w \tag{C8}$$

where E_s is the elastic modulus of the soil-solid part.

Data availability

Data will be made available on request.

References

[1] Deal E, Venditti JG, Benavides SJ, Bradley R, Zhang Q, Kamrin K, Perron JT. Grain shape effects in bed load sediment transport. Nature 2023;613(7943):298–302.
[2] Garoosi F, Mellado-Cusicahua AN, Shademani M, Shakibaeinia A. Experimental and numerical investigations of dam break flow over dry and wet beds. Int J Mech Sci 2022;215:106946.
[3] Lu C, Cheng NS. Experimental measurements of sediment pickup probability at low transport stage. J Geophys Res 2025;130(6). e2024JF008222.
[4] Barneveld HJ, Frings RM, Mosselman E, Venditti JG, Kleinhans MG, Blom A, Hoitink AJF. Extreme river flood exposes latent erosion risk. Nature 2025;644 (8076):391–7.
[5] Hassan MA, Pierce JK, Chartrand SM. Sediment storage and fluvial sediment transport linkages across an experimental flood sequence. J Geophys Res 2024;129 (9). e2024JF007772.
[6] Menezes D, Borges ALO. Bed roughness in gravel-bed rivers: channel-scale responses to flow and sediment dynamics. Adv Water Resour 2025:105146.
[7] Inagaki N, Shibayama T, Nakamura R, Ishibashi K, Esteban M. Experimental investigation into the effects of strong winds on the transport of overtopping water mass over a vertical seawall. Coastal Eng J 2024;66(2):201–15.
[8] Taskaya E, Bombar G, Tayfur G. Experimental investigation of sediment movement as a result of homogeneous earth-fill dam overtopping break over a simplified urban area. J Hydrol 2023;617:128924.
[9] Zhou GG, Li S, Lu X, Tang H. Large-scale landslide dam breach experiments: overtopping and "overtopping and seepage" failures. Eng Geol 2022;304:106680.
[10] Cho Y, Nakamura T, Mizutani N, Sugimoto W. Small ship collisions in coastal areas during tsunamis: impact on seawalls behind sand dunes. Coast Eng 2024;189: 104486.
[11] Hayashizaki S, Kawajiri S, Kurokawa T, Ogasawara A, Kawaguchi T, Nakamura D, Minabe Y. Experimental study on erosion process of expressway embankment subjected to tsunami after earthquake. Transp Infrastruct Geotechnol 2024;11(5): 3062–77.
[12] Sajan MK, Chaudhary B, Sah B. Investigations on the development of hybrid mound breakwaters for tsunami defense. Appl Ocean Res 2025;156:104489.
[13] Liu C, Shan Y, He L, Li F, Liu X, Nepf H. Plant morphology impacts bedload sediment transport. Geophys Res Lett 2024;51(12). e2024GL108800.
[14] Feng H, Yin ZY, Liang W. A novel unified elastoplasticity-μ(I) phase transition model for granular flows from solid-like to fluid-like states and its application. Eng Geol 2025;352:108054.
[15] Barrie A, Wang C, Liang F, Qi W. Experimental investigation on the mechanism of local scour around a cylindrical coastal pile foundation considering sloping bed conditions. Ocean Eng 2024;312:119225.
[16] Cúñez FD, Franklin EM, Houssais M, Arratia P, Jerolmack DJ. Strain hardening by sediment transport. Phys Rev Res 2022;4(2):L022055.
[17] Shields A. Anwendung der aehnlichkeitsmechanik und der turbulenzforschung auf die geschiebebewegung. PhD Thesis. Technical University Berlin; 1936.
[18] Kinnell PIA. Insights into the sediment transport processes operating in rain-impacted flows. Catena (Amst) 2022;217:106452.
[19] Russell CE, Fernández R, Parsons DR, Gabbott SE. Plastic pollution in riverbeds fundamentally affects natural sand transport processes. Commun Earth Environ 2023;4(1):255.
[20] Serra T, Soler M, Barcelona A, Colomer J. Suspended sediment transport and deposition in sediment-replenished artificial floods in Mediterranean rivers. J Hydrol 2022;609:127756.
[21] Shu J, Liu Z, Jiang B, Guo H. Experimental study on the suspended sediment settlement characteristics and incipient velocity in the straight-line sedimentation basin of the irrigation headworks. Can Geotechnical J 2025;62:1–17.
[22] Dasent J, Wright V, Scharer K, Manga M, Kilburn R. Memory and jamming in fault zone sediments. Commun Earth Environ 2025;6(1):998.
[23] Bodek S, Wang D, Shattuck MD, O'Hern CS, Ouellette NT. Anisotropic stress history effects in erodible sediment beds. J Geophys Res 2026;131(1). e2025JF008561.
[24] Khosronejad A, Kang S, Sotiropoulos F. Experimental and computational investigation of local scour around bridge piers. Adv Water Resour 2012;37:73–85.
[25] Qu L, An H, Draper S, Watson P, Cheng L. An experimental investigation of local scour at squat, shallowly embedded subsea structures. Coast Eng 2025:104851.
[26] Roelofs L, Nota EW, Flipsen TC, Colucci P, de Haas T. How bed composition affects erosion by debris flows-an experimental assessment. Geophys Res Lett 2023;50 (14). e2023GL103294.
[27] Zhang Y, Chen G, Hu J, Chen X, Yang W, Tao A, Zheng J. Experimental study on mechanism of sea-dike failure due to wave overtopping. Appl Ocean Res 2017;68: 171–81.
[28] Cook BK, Noble DR, Williams JR. A direct simulation method for particle-fluid systems. Eng Comput (Swansea) 2004;21(2/3/4):151–68.
[29] Zhang P, Mu L, Lu Y, Huang M, Sun J. Microscopic insights into suction bucket installation in sand: coupled coarse-grained CFD-DEM simulations. Comput Geotech 2024;167:106060.
[30] Zhang S, Li B, Ma H. Numerical investigation of scour around the monopile using CFD-DEM coupling method. Coast Eng 2023;183:104334.
[31] Zhao Z, Zhou L, Bai L, Wang B, Agarwal R. Recent advances and perspectives of CFD–DEM simulation in fluidized bed. Arch Comput Methods Eng 2024;31(2): 871–918.
[32] Luo M, Su X, Kazemi E, Jin X, Khayyer A. Review of smoothed particle hydrodynamics modeling of fluid flows in porous media with a focus on hydraulic, coastal, and ocean engineering applications. Phys Fluids 2025;37(2).
[33] Peng Y, Yin ZY. Micromechanical analysis of local scour behaviors around circular piles in granular soil under steady flows with SPH-DEM. Ocean Eng 2025:328.
[34] Su Z, Wang S, Li D, Sheng J, Wu W. SPH–DEM modeling overtopping failure of earthfill dams. Acta Geotech 2024;19(2):953–70.
[35] Baumgarten AS, Couchman BL, Kamrin K. A coupled finite volume and material point method for two-phase simulation of liquid–sediment and gas-sediment flows. Comput Methods Appl Mech Eng 2021;384:113940.
[36] Feng H, Yin ZY, Peng M, Guo Q. State-of-the-art review of continuum mechanics-based modelling of soil surface erosion: state-of-the-art review of continuum mechanics-based modelling of soil surface erosion. Arch Comput Methods Eng 2025;32(4):1969–95.
[37] Baykal C, Sumer BM, Fuhrman DR, Jacobsen NG, Fredsøe J. Numerical simulation of scour and backfilling processes around a circular pile in waves. Coast Eng 2017; 122:87–107.
[38] Burkow M, Griebel M. A full three dimensional numerical simulation of the sediment transport and the scouring at a rectangular obstacle. Comput Fluids 2016; 125:1–10.
[39] Gothel O. Numerical modeling of flow and waveinduced scour around vertical structures. PhD thesis. Hanover: Leibniz University of Hanover, Faculty of Civil Engineering and Geodesy; 2008.
[40] Liu MM, Wang HC, Tang GQ, Shao FF, Jin X. Investigation of local scour around two vertical piles by using numerical method. Ocean Eng 2022;244:110405.
[41] Liu Y, Huang M, Yu J. Three-dimensional numerical analysis of local scour around inclined twin piles with varying current directions. Ocean Eng 2025;335:121631.
[42] Roulund A, Sumer BM, Fredsøe J, Michelsen J. Numerical and experimental investigation of flow and scour around a circular pile. J Fluid Mech 2005;534: 351–401.
[43] Chen J, Sun S, Wang X. Homogenization of two-phase fluid flow in porous media via volume averaging. J Comput Appl Math 2019;353:265–82.
[44] Bhatti MM, Marin M, Zeeshan A, Abdelsalam SI. Recent trends in computational fluid dynamics. Front Phys 2020;8:593111.
[45] Hong Y, Yang X, Liu K, Wu Y, Wu Y. Adaptive resolution SPH method for non-Newtonian slurry mixing. Int J Mech Sci 2025;289:110053.
[46] Hu Z, Liu Y, Zhang Z, Ye H, Zhang H, Zheng Y. Coupling explicit phase-field MPM for two-dimensional hydromechanical fracture in poro-elastoplastic media. Int J Mech Sci 2023;260:108649.
[47] Xu T, Jin YC, Tai YC. Peridynamic mesh-free simulation of glass and metal beads column collapses. Int J Mech Sci 2023;256:108485.
[48] Xie F, Pan G, Zhao W, Wan D. Unresolved MPS-DEM coupling method for three-dimensional liquid-solid dam-break flows impacting on rigid structures. Ocean Eng 2025;323:120601.
[49] Tang XQ, Alibrandi U, Koh CG. Numerical simulation of sediment erosion and transport using consistent particle method. Adv Water Resour 2025;205:105105.
[50] Tang ZQ, Jin YF, Yang J, Yin ZY, Chen X. Multi-physics two-layer SNS-PFEM for granular mass-water large deformation problems. Int J Mech Sci 2025:110492.
[51] Amoudry L, Hsu TJ, Liu PF. Two-phase model for sand transport in sheet flow regime. J Geophys Res 2008;113(C3).
[52] Mathieu A, Chauchat J, Bonamy C, Nagel T. Two-phase flow simulation of tunnel and lee-wake erosion of scour below a submarine pipeline. Water (Basel) 2019;11 (8):1727.
[53] Nagel T, Chauchat J, Bonamy C, Liu X, Cheng Z, Hsu TJ. Three-dimensional scour simulations with a two-phase flow model. Adv Water Resour 2020;138:103544.
[54] Galano N, Moreno-Casas PA, Abell JA. Extending the particle finite element method for sediment transport simulation. Comput Methods Appl Mech Eng 2021; 380:113772.
[55] Oñate E, Celigueta MA, Idelsohn SR, Salazar F, Suárez B. Possibilities of the particle finite element method for fluid–soil–structure interaction problems. Comput Mech 2011;48(3):307–18.
[56] Rubin MB, Ciambella J, Nadler B. A continuum model for granular materials exhibiting a smooth transition between inelastic flow and elastic jamming. Int J Mech Sci 2024;277:109391.
[57] Wang D, Li S, Arikawa T, Gen H. ISPH simulation of scour behind seawall due to continuous tsunami overflow. Coastal Eng J 2016;58(03):1650014.
[58] Zhou M, Shi Z, Peng C, Peng M, Cui KFE, Li B, Zhou GG. Two-phase modelling of erosion and deposition process during overtopping failure of landslide dams using GPU-accelerated ED-SPH. Comput Geotech 2024;166:105944.
[59] Zubeldia EH, Fourtakas G, Rogers BD, Farias MM. Multi-phase SPH model for simulation of erosion and scouring by means of the shields and Drucker–Prager criteria. Adv Water Resour 2018;117:98–114.
[60] Liang D, Zhao X, Soga K. Simulation of overtopping and seepage induced dike failure using two-point MPM. Soils Found 2020;60(4):978–88.
[61] Yamaguchi Y, Takase S, Moriguchi S, Terada K. Solid–liquid coupled material point method for simulation of ground collapse with fluidization. Comput Part Mech 2020;7(2):209–23.
[62] Abe K, Soga K, Bandara S. Material point method for coupled hydromechanical problems. J Geotech Geoenviron Eng 2014;140(3):04013033.
[63] Bandara S, Soga K. Coupling of soil deformation and pore fluid flow using material point method. Comput Geotech 2015;63:199–214.

[64] Gao M, Pradhana A, Han X, Guo Q, Kot G, Sifakis E, Jiang C. Animating fluid sediment mixture in particle-laden flows. ACM Trans Graphics (TOG) 2018;37(4):1–11.
[65] Mackenzie-Helnwein P, Arduino P, Shin W, Moore JA, Miller GR. Modeling strategies for multiphase drag interactions using the material point method. Int J Numer Methods Eng 2010;83(3):295–322.
[66] Tampubolon AP, Gast T, Klár G, Fu C, Teran J, Jiang C, Museth K. Multi-species simulation of porous sand and water mixtures. ACM Trans Graphics (TOG) 2017;36(4):1–11.
[67] Liang D, Zhao X, Martinelli M. MPM simulations of the interaction between water jet and soil bed. Procedia Eng 2017;175:242–9.
[68] Ng CWW, Jia Z, Poudyal S, Bhatta A, Liu H. Two-phase MPM modelling of debris flow impact against dual rigid barriers. Géotechnique 2023;74(12):1390–403.
[69] He KY, Jin YF, Zhou XW, Yin ZY. A high-performance semi-implicit two-phase two-layer MPM framework for modeling granular mass-water interaction problems. Comput Methods Appl Mech Eng 2024;427:117064.
[70] Anderson TB, Jackson R. Fluid mechanical description of fluidized beds. Equations of motion. Ind Eng Chem Fundam 1967;6(4):527–39.
[71] Crowe CT, Troutt TR, Chung J. Numerical models for two-phase turbulent flows. Annu Rev Fluid Mech 1996;28(1):11–43.
[72] Ibrahim A, Meguid MA. Coupled flow modelling in geotechnical and ground engineering: an overview. Int J Geosynthetics Ground Eng 2020;6:1–25.
[73] Pudasaini SP, Fischer JT. A mechanical erosion model for two-phase mass flows. Int J Multiph Flow 2020;132:103416.
[74] Van Deemter JT, Van der Laan ET. Momentum and energy balances for dispersed two-phase flow. Appl Scientif Res 1961;10:102–8.
[75] Zou S, Huang M, Shi Z. Evaluation of wave-induced flow through marine porous media accounting for transition of seepage properties across multiple flow regimes. Appl Ocean Res 2025;154:104346.
[76] Drucker DC, Prager W. Soil mechanics and plastic analysis or limit design. Q Appl Math 1952;10(2):157–65.
[77] Huang M, Chen Z, Lu X. Bifurcation prediction of shear banding in sand with non-coaxial critical state model considering inherent anisotropy. Soils Found 2018;58(3):641–53.
[78] Yin ZY, Hicher PY, Dano C, Jin YF. Modeling mechanical behavior of very coarse granular materials. J Eng Mech 2017;143(1):C4016006.
[79] Wu W, Bauer E. A simple hypoplastic constitutive model for sand. Int J Numer Anal Methods Geomech 1994;18(12):833–62.
[80] Wu W, Lin J, Wang X. A basic hypoplastic constitutive model for sand. Acta Geotech 2017;12:1373–82.
[81] Da Cruz F, Emam S, Prochnow M, Roux JN, Chevoir F. Rheophysics of dense granular materials: discrete simulation of plane shear flows. Phys Rev E-Statistical Nonlinear Soft Matter Phys 2005;72(2):021309.
[82] Daniel RC, Poloski AP, Sáez AE. A continuum constitutive model for cohesionless granular flows. Chem Eng Sci 2007;62(5):1343–50.
[83] Jop P, Forterre Y, Pouliquen O. A constitutive law for dense granular flows. Nature 2006;441(7094):727–30.
[84] Allen B, Kudrolli A. Depth resolved granular transport driven by shearing fluid flow. Phys Rev Fluids 2017;2(2):024304.
[85] Maurin R, Chauchat J, Frey P. Dense granular flow rheology in turbulent bedload transport. J Fluid Mech 2016;804:490–512.
[86] Gens A, Potts DM. Critical state models in computational geomechanics. Eng Comput (Swansea) 1988;5(3):178–97.
[87] Zhao X, Bolognin M, Liang D, Rohe A, Vardon PJ. Development of in/outflow boundary conditions for MPM simulation of uniform and non-uniform open channel flows. Comput Fluids 2019;179:27–33.
[88] Daly E, Grimaldi S, Bui HH. Explicit incompressible SPH algorithm for free-surface flow modelling: a comparison with weakly compressible schemes. Adv Water Resour 2016;97:156–67.
[89] Zhang X, Oñate E, Torres SAG, Bleyer J, Krabbenhoft K. A unified Lagrangian formulation for solid and fluid dynamics and its possibility for modelling submarine landslides and their consequences. Comput Methods Appl Mech Eng 2019;343:314–38.
[90] Khanpour M, Zarrati AR, Kolahdoozan M, Shakibaeinia A, Amirshahi SM. Mesh-free SPH modeling of sediment scouring and flushing. Comput Fluids 2016;129:67–78.
[91] Nikeghbali P, Benjankar R, Kheirkhahan M. Erosion under drawdown flushing with the SPH method. Ocean Eng 2024;310:118743.
[92] Schmocker L. Hydraulics of dike breaching, 218. VAW-Mitteilungen; 2011.
[93] Arikawa T, Ikeda T, Kubota K. Experimental study on scour behind seawall due to tsunami overflow. J Japan Soc Civil Engineers 2014. Ser. B, 2.
[94] Li S, Arikawa T, Wang D, Gen H. Numerical simulation on scour behind seawalls due to Tsunami overflow. Coastal Struct Sol Coastal Disasters 2017;2015.
[95] Rijn LCV. Sediment transport, part II: suspended load transport. J Hydraulic Eng 1984;110(11):1613–41.
[96] Annandale GW. Scour technology: mechanics and engineering practice. McGraw Hill Professional; 2006.